

University of Crete

Master Thesis

**Simultaneous Optical/Ultraviolet/X-ray
variability study of NGC 5548**

Author:
Christos Panagiotou

Supervisor:
Prof. Iossif Papadakis

School of Science and Engineering
Department of Physics

Heraklion, July 20, 2016

Abstract

Active Galactic Nuclei (AGN) are luminous and exotic celestial objects. It is generally accepted that AGN are powered by the accretion of mass onto a super-massive black hole, which is located at their center. As matter accretes in the form of a disk, energy is liberated and radiated as black body emission in the optical and ultraviolet wavebands. The observed X-rays of AGN are considered to be the result of thermal Comptonization of soft photons in a hot plasma region, usually called the X-ray "corona".

Despite being extensively studied for more than 40 years, many of the physical processes in AGN are still unclear. A reason for that is the really small (angular) size of the AGN, which does not allow a direct observation of their core region with the currently used instruments. As a result, the only way to get information about those objects is the simultaneous multi-wavelength observations.

The results from such studies so far have been suggestive, and not conclusive. In general, the ultraviolet/optical emission is well correlated, with delays which increase with the wavelength. However, the correlation between X-ray and ultraviolet variations is rather low. The corresponding time lag suggests that X-ray variations lead the ultraviolet/optical ones, although the results are also consistent, within the errors, with the ultraviolet emission leading the X-rays.

A possible explanation of the small correlation between the X-rays and the ultraviolet flux is that the observed X-rays (in 0.3–10 keV) are combination of the *intrinsic* X-ray emission (i.e. the corona emission) and the interaction of this emission with a photo-ionized absorbing material, namely the "warm absorber". As a result, the observed X-ray variability is partly due to the variations of the corona emission and partly due to the variations of the absorber's properties.

In this work I analyzed the observations of NGC 5548 obtained by the Swift observatory from February, 17th to June, 22nd, 2014. I fitted the X-ray spectra with a proper theoretical model and I managed to determine the intrinsic X-ray flux of the source. Then, I cross-correlated this flux with the ultraviolet lightcurve. I found that the correlation coefficient is rather low and the time lag suggests that the X-rays lead the ultraviolet variations by ~ 6 days. The X-ray and ultraviolet correlation is very large ($DCF \sim 0.85$) during the first part of the lightcurves, which show a clear, large-amplitude "flare". This is suggestive of accretion rate (\dot{m}) variations in the inner part of the disk, which creates sound waves propagating outwards. There is no observed correlations between the two fluxes in the second half of the observations. Finally, the correlation analysis indicate that the w2 ultraviolet photons ($\lambda_{eff} = 2030\text{\AA}$) are not the soft input photons that produce the X-rays.

Acknowledgements

I wish to express my gratitude to my supervisor, Professor Iossif Papadakis, for his guidance, patience and belief in my abilities. I also want to express my thanks to my colleagues and friends, mainly graduate students of the department, for sharing their knowledge with me and for their support. Finally, special thanks should be awarded to my family for their financial and moral support.

Contents

1	Introduction	7
1.1	Characteristics of an Active Galactic Nucleus	7
1.2	The central engine	9
1.3	X-rays from AGN	11
1.4	NGC 5548	12
1.5	The main objective of the study	15
2	Data analysis	17
2.1	The 'SWIFT' mission	17
2.2	The Swift monitoring of NGC5548	18
2.3	X-ray Data Reduction	19
2.4	Observations Grouping	21
3	X-ray Spectral Modelling	25
3.1	The X-ray model	25
3.2	Model fit: Stage 1	26
3.3	Model fit: Stage 2	27
3.4	Model fit: Stage 3	27
3.5	The warm absorber parameters	30
3.6	The X-ray continuum model parameters	31
4	Correlation analysis	35
4.1	The Cross-Correlation Function	35
4.2	The intrinsic X-ray/UV correlation in NGC 5548	36
4.3	The Γ /UV correlation in NGC 5548	40
5	Summary and Conclusions	43
5.1	Summary of the work	43
5.2	Conclusions	44
	References	47

Chapter 1

Introduction

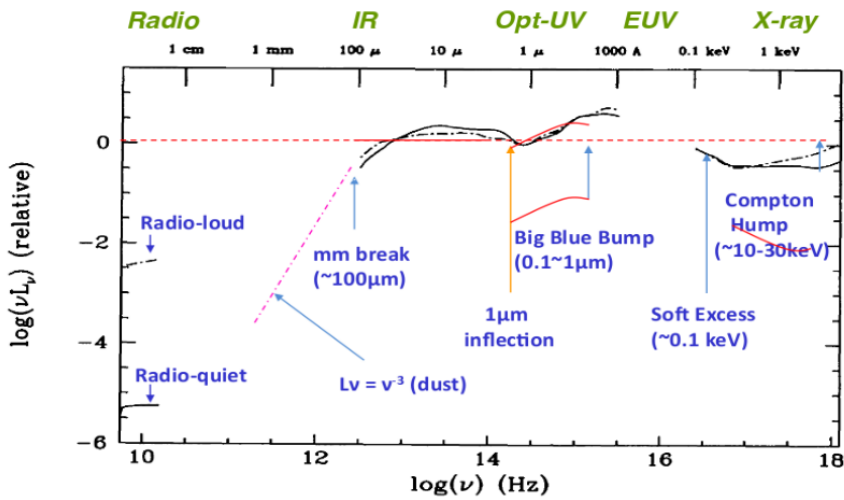
1.1 Characteristics of an Active Galactic Nucleus

Active galaxies are a class of galaxies showing energetic activity not observed in normal galaxies. This activity takes place in their central region and it cannot be attributed directly to stars. The core region of an active galaxy is called Active Galactic Nucleus (AGN). The AGN present numerous interesting characteristics.

Continuum Emission

The typical spectrum of an AGN is shown in Fig. 1.1. The most notable feature is that the AGN radiation spans from radiowaves to hard X-rays and even to γ -rays in some AGN. The spectral energy distribution (SED) appears to be flat, within an order of magnitude, from infrared wavelengths to X-rays. The observed SED cannot be explained by stellar radiation, not even a sum of them, and cannot, therefore, be attributed to emission by stars. The bolometric luminosity of an AGN is of the order 10^{43} erg/s to 10^{49} erg/s and thus in many cases it exceeds the luminosity of the host galaxy, which is of the order of $\sim 10^{44}$ erg/s.

Figure 1.1: The SED of an AGN (Elvis et al. 1994). The solid black line corresponds to the spectrum of the radio-quiet AGN.



Another unique feature in the AGN SED is the so-called 'Big Blue Bump' (BBB, see Fig. 1.1). The BBB is the increase of the emitted power in the blue and ultraviolet waveband. This is another indication that the AGN radiation cannot be attributed to stellar emission, since even the hottest stars show a power decrease in this waveband. The BBB can be

explained by thermal emission of gas accreting onto a super-massive black hole (BH), in a form of a disk (see § 1.2).

Emission Lines

Strong emission lines of abundant elements (like hydrogen, oxygen, carbon etc.) are present in the ultraviolet-optical spectra of AGN. These lines are divided into two categories, the 'broad' and the 'narrow' emission lines, depending on their widths. The observed widths are considered to be the result of the Doppler-broadening of the lines due to their motion with respect to the central object. The widths of the broad lines are of the order of $\sim 10^3 - 10^4$ km/s, while the widths of the narrow lines are considerably smaller, $\sim 10^2 - 10^3$ km/s. This suggests that the broad lines are emitted by a region (the Broad Line Region, BLR) which is much closer to the center of the AGN compared to the Narrow Line Region (NLR). Moreover, some of the observed narrow lines correspond to forbidden transitions, which is not the case for the broad lines. The observed lines also indicate that the gas in BLR is in higher ionization state than the gas in NLR. Thus, BLR is hotter and denser than NLR. Both regions are thought to be photoionized by the continuum emission of the central source.

The AGN emission lines have been studied extensively for many years in order to obtain information for the two line regions as well as for the overall structure of the nuclei. "Reverberation mapping" studies (i.e. studies of the correlation between the broad lines and the continuum emission variations) indicate that a massive object is located in the central region of AGN, with typical masses of $\sim 10^7$ to $10^8 M_{\odot}$.

Variability

AGN radiation is variable over the whole electromagnetic spectrum. The characteristic variability timescale increases with the wavelength. Specifically, X-rays vary by a factor of ~ 2 or more in times of a few minutes to less than a day, the ultraviolet-optical radiation is observed to vary in timescales of a day to a few weeks and the variability timescale of infrared emission is of the order of years. The different timescales suggest that the size of the various emission components in AGN increases with the wavelength. An upper limit on the size of the emitting regions can be estimated using the simple argument that a variable source cannot be larger than the distance travelled by light in the corresponding time. Hence, the radius of the X-ray source should be a few light-travel minutes/hours, maximum, and the ultraviolet-optical region should be about 10 to 100 times bigger.

To recap, most AGN emit power larger than the emitted power of their host galaxies. Most of this power is emitted in regions with a size similar to the size of our solar system (based on variability arguments). The widths of the broad lines suggest the presence of more than a few million solar mass object in this small region. These characteristics indicate that the physical processes which operate in an AGN must be different than those in typical galaxies. Lots of research work has been done in the past in order to develop appropriate models that propose plausible mechanism which can explain the observational characteristics in AGN.

1.2 The central engine

According to the currently accepted model, a supermassive black hole ($M_{\text{BH}} > 10^6 M_{\odot}$) is located in the centre of every active galactic nucleus. The mechanism that powers the AGN is the accretion of matter onto this black hole in the form of a disk. The disk is formed as follows. As particles approach the black hole, they are attracted by its gravitational potential. Since the particles have, in general, an initial angular momentum with respect to the BH, they will start to move into elliptical orbits around it. As more and more gaseous particles are concentrated around the black hole, their orbits will be intersected and hence, they will collide and exchange angular momentum. The whole procedure is expected to lead eventually to a stable configuration, where an accretion disk is formed.

The disk luminosity

The accretion of mass onto a black hole can in principle account for the enormous amounts of luminosity emitted by AGN. Assume that a particle with mass m is left to fall from infinity onto the black hole. The maximum energy that could be radiated during this process is equal to the amount of gravitational potential energy gained by that particle. This potential energy for a particle moving from infinity to a $3R_S$ -radius¹ orbit, which is the inner stable circular orbit for a Schwarzschild black hole, is equal to:

$$U = G \frac{mM_{\text{BH}}}{3R_S} \quad (1.1)$$

where M_{BH} is the black hole mass. Assuming that mass is continuously accreting to the BH, with a rate of $\dot{m} = \frac{dm}{dt}$, the maximum luminosity that can be radiated through accretion is:

$$L = \frac{dU}{dt} \simeq 0.17\dot{m}c^2 \quad (1.2)$$

The arithmetic coefficient in equation (1.2) is called "efficiency", ϵ , and is a measure of the fraction of the particle's rest energy that is radiated. In the case of a maximally rotating (Kerr) black hole, the efficiency could be as large as 0.4. Comparing this to the corresponding value for the nuclear fusion in the stars, $\epsilon = 0.008$, it is obvious that accretion is a much more efficient process. According to equation (1.2) the typical AGN luminosity, $L \simeq 10^{45}$ erg/s, can be achieved by an accretion rate of $\sim 7 \cdot 10^{21}$ kg/s. Assuming a central black hole mass of $M_{\text{BH}} \geq 10^6 M_{\odot}$, the above calculated accretion rate is smaller than the Eddington rate for this mass.

The Eddington mass rate is the accretion rate that corresponds to the Eddington limit, which is the luminosity emitted in the limiting case when the outward radiation force and the inward gravitational force are equal. Consequently the accretion of mass onto a supermassive BH can in principle explain the observed luminosity value.

¹ R_S is the Schwarzschild radius, $R_S = \frac{2GM_{\text{BH}}}{c^2}$

The accretion disk spectrum

After the disk is formed, mass is orbiting in nearly co-planar circular orbits around the black hole. Due to viscosity (whose nature is not understood yet) mass in small annuli at distance R from the BH lose angular momentum; and moves inwards (for the total angular momentum to be conserved a small portion of the accreting mass should be moved outwards, far from the center.) In this way, gravitational energy is liberated. Assuming that the released energy is locally dissipated and, in addition, that the disk is optically thick, each annulus will emit a black body radiation. As a result, the total radiation of the disk will be equal to the sum of the emission of the various annuli which emit as black bodies. Thus, in order to estimate the expected spectrum, it is sufficient to calculate the temperature profile of the disk. This can be done as follows.

Let us consider a particle of mass m at distance $R+\Delta R$, which, due to viscosity, moves towards to the black hole by ΔR . Its potential energy will be approximately decreased by:

$$\Delta E \simeq \frac{GmM_{BH}}{R^2} \Delta R \quad (1.3)$$

This is the maximum available energy in the system. Following the virial theorem, half of this energy will be used to increase the kinetic energy of the gas and thus heats the disk, while the other half is radiated away. Consider now all the mass in an annulus of width ΔR at distance R . Since each annulus emits as a black body, according to the Stefan-Boltzmann law, the luminosity emitted by this annulus is:

$$L(R) = 2\pi R \Delta R \sigma T^4(R) \quad (1.4)$$

where σ is the Stefan-Boltzmann constant. Combining equations (1.3) and (1.4), we find that:

$$T(R) = \left(\frac{GM_{BH}\dot{m}}{4\pi\sigma R^3} \right)^{1/4} \quad (1.5)$$

A more precise derivation results in the following equation for the disk temperature:

$$T(R) = \left\{ \frac{3GM_{BH}\dot{m}}{8\pi\sigma R^3} \left[1 - \left(\frac{R_{in}}{R} \right)^{1/2} \right] \right\}^{1/4} \quad (1.6)$$

R_{in} is the inner radius of the disk. For $R \gg R_{in}$ equation (1.6) is reduced to:

$$T(R) \simeq 2.8 \cdot 10^5 K \left(\frac{M_{BH}}{10^8 M_{\odot}} \right)^{-1/4} \left(\frac{\dot{m}}{\dot{m}_{Edd}} \right)^{1/4} \left(\frac{R}{3R_S} \right)^{-3/4} \quad (1.7)$$

The above equation indicates that the temperature of the disk increases with the accretion rate; while for a given accretion rate, the temperature decreases as the BH mass increases. Finally for given BH mass and accretion rate, the temperature increases as moving closer to the black hole. For typical values of the AGN luminosity, $L \simeq 10^{45}$ erg/s, and $\dot{m} = 0.05\dot{m}_{Edd}$, equation (1.6) results that the maximum temperature of the disk is $\sim 10^5$ Kelvin, which corresponds to black body emission peaked at 300\AA .

To sum up, the disk emission can be considered as the sum of the radiation emitted by the different disk annuli. Each annulus radiates as a black body with a characteristic temperature given by equation (1.6). This temperature can be as high as $\sim 10^5$ Kelvin in the inner regions of the disk and thus, the corresponding spectrum will present a peak in the extreme UV (i.e. ultraviolet) waveband. This is thought to be a plausible explanation for the "big blue bump" feature, which is observed in the AGN spectra. The overall emission of the disk is usually called "disk-blackbody radiation".

The successful explanation of the BBB and the large luminosity of AGN are two of the main reasons why the accretion model is currently accepted as the most plausible mechanism for the optical/ultraviolet emission in AGN.

1.3 X-rays from AGN

The X-ray spectrum

AGN are luminous X-ray sources. In fact, their observed X-ray luminosity is so high (typically more than 10^{42} erg/s), that this feature is currently used as a defining characteristic of an AGN. Since the disk temperature is not high enough for the disk to emit X-rays, an additional mechanism must operate in the innermost region of AGN.

It is currently believed that X-rays are the result of Comptonization of low-energy photons by electrons in a hot plasma, with a temperature ~ 100 keV. The hot plasma region is usually called as the "corona". This mechanism results in a power-law spectrum with a cutoff at energy representative of the corona temperature. It is also believed that the soft input photons are the photons emitted by the disk.

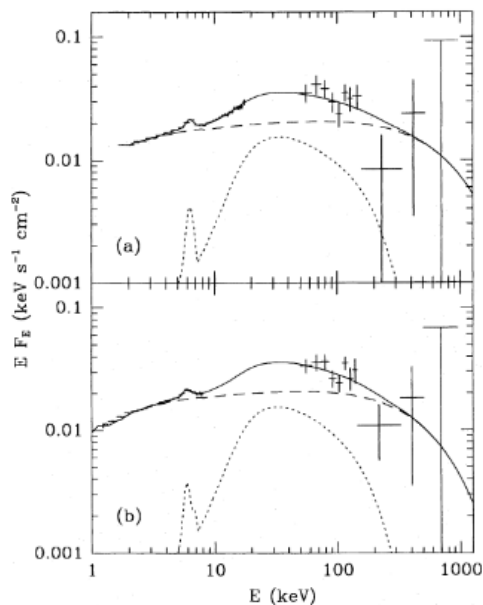


Figure 1.2: The average X-ray spectrum of Type 1 AGN (Gondek et al. 1996). The dashed lines correspond to a power-law spectrum with an exponential cutoff (and bound-free absorption at low energies). The dotted lines represent the 'Compton reflection' spectrum, with the Fe K α line being prominent. Top: The spectrum using data from Ginga and OSSE (Oriented Scintillation Spectrometer Experiment). Bottom: The spectrum using data from EXOSAT (European X-ray Observatory Satellite) and OSSE.

This interpretation is supported by the shape of the X-ray spectrum in AGN. The typical spectrum of the radio-quiet Type 1 AGN in energies above 2 keV is shown in Fig. 1.2. The

solid black lines represent the mean X-ray spectral energy distribution of the AGN. The dashed lines represent the spectral component that corresponds to the thermal Comptonization and the dotted line corresponds to the "X-ray reflection" component.

The photons scattered in the corona are emitted at all directions. Thus, the corona emission is expected to also illuminate the disk. The corona photons are expected to interact with the disk gas through Compton scattering and photoelectric absorption. The combinations of these effects results in the "X-ray reflection" component of the AGN spectrum. Due to Compton scattering high-energy photons (with energies above 50 keV) lose energy and are observed in lower frequencies between 20 to 50 keV. The above mentioned procedure is thought to produce the so-called "hump" feature observed in the X-ray spectrum of an AGN (dotted line in Fig. 1.2). Furthermore, the photons with lower energy ($<10\text{keV}$) are absorbed by ions, which then emit emission lines, with the most characteristic example being the Fe K α line at 6.4keV. An observed X-ray reflection component could also be produced by the interaction between the X-ray photons and the dusty torus, which may be located light months away from the center of the AGN.

The "warm absorber"

Another interesting feature of AGN is the detection of absorption lines in their X-ray spectra, at energies typically smaller than 1–2keV. George et al. (1998) and Crenshaw et al. (2003) showed that those lines are present in the spectra of more than 50% of Type 1 AGN. The lines are thought to be the result of the photoionization of a region, the so-called "warm absorber" region, probably by the corona continuum emission itself. The warm absorber lies along the line of sight towards the central engine of the AGN. In many cases the absorbing gas is outflowing, with velocities ranging from a few hundred km/s to 10^4 km/s and a corresponding large column density from 10^{21} to 10^{24} cm $^{-2}$. The warm absorber may also result in absorption lines in the ultraviolet waveband, as well, which has also been observed (Crenshaw et al. 1999).

Despite the numerous studies investigating the warm absorber's characteristics that have been conducted since its identification, our understanding of its properties (location, density etc) is still poor. As a result, many aspects concerning the physics of the warm absorber, like its origin and energetics, are still unclear.

1.4 NGC 5548

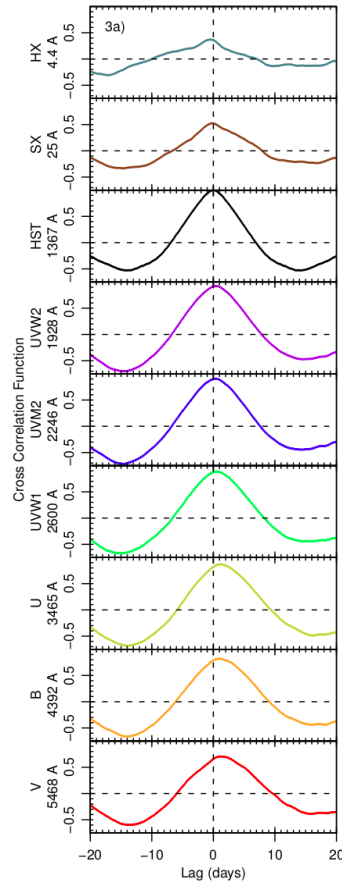
The AGN I studied in this work is the Type 1 Seyfert galaxy NGC 5548. NGC 5548 is one of the best studied active galaxies. It is an X-ray bright AGN at $z = 0.017175$ (de Vaucouleurs et al. 1991). Its black hole mass was estimated to be $M_{\text{BH}} = 5.2 \cdot 10^7 M_{\odot}$ (Bentz et al. 2015).

Previous studies (see Steenbrugge et al. 2005 and references therein) have detected absorption lines in the X-ray spectrum of NGC 5548, indicative of the presence of warm absorber. Ebrero et al. (2016) suggested that the warm absorber in this object is composed of six different ionization phases, located at ~ 0.4 to a few pc from the central ionizing source. Another recent work (Kaastra et al. 2014) revealed that the absorbing properties of NGC 5548 are more complicated. They deduced that the soft X-rays are absorbed by two distinct components, a warm absorber and an "obscuration" component. The obscuring gas is located closer

to the nucleus than the warm absorber. This "obscurer" consists of gaseous atoms that are in a low ionization state and are thought to be originated by the disk.

Ursini et al. (2015) have used observations obtained by XMM-Newton, Chandra, NuSTAR and INTEGRAL, to study the X-ray spectrum of NGC 5548. They found that the observed spectrum above 5keV can be reproduced by a power-law with an exponential cut-off model plus an X-ray reflection spectral component. The photon index of the power-law varied from ~ 1.5 to ~ 1.7 and the energy cut-off was always larger than 50 keV. They also estimated that the corona temperature was highly variable with a mean value $T = 40^{+40}_{-10}$ keV.

Figure 1.3: The optical/UV/X-ray CCF of NGC 5548, as estimated by Edelson et al. (2015). The different panels from top to bottom correspond to the CCFs (with respect to the Hubble Space Telescope, HST, flux) of: hard X-rays, soft X-rays, HST (auto-correlation), w2 filter, m2 filter, w1 filter, u filter, b filter and v filter, respectively.



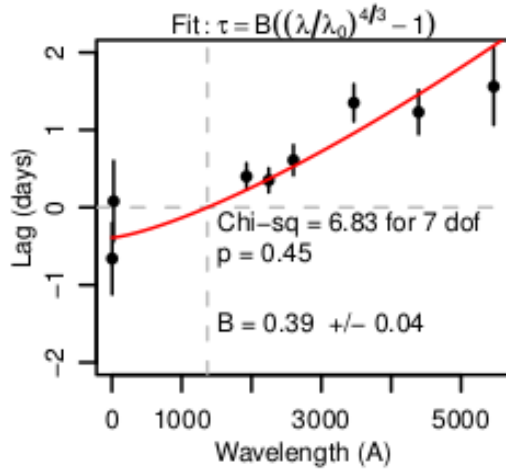
The 2014 Swift campaign

The ultraviolet-optical and X-ray emission of NGC 5548, is known to be variable at all timescales. Edelson et al. 2015 (E15, hereafter) studied in detail those variation using multi-

wavelength observations obtained by the Swift observatory and the Hubble Space Telescope (HST). In fact, Swift observed ~ 280 times from February, 17th to June, 22nd 2014 (for details see Chapter 2). The importance of this study lies on the quality of the resulting lightcurves. The 2014 Swift monitoring campaign of NGC 5548 resulted in lightcurves that are, arguably, the densest, simultaneous optical/UV/X-ray lightcurves ever obtained for an AGN, on time scales of a few months.

E15 used those observations to investigate the interband correlations. To that end, they estimated the cross-correlation function (CCF) of the lightcurves in the various wavebands with the observed HST lightcurve as the reference one. The correlation functions, as calculated in the above study, are shown in Fig. 1.3. "HX" stands for the hard X-rays with energy above 0.8 keV and "SX" for the soft X-rays with energy from 0.3 to 0.8 keV. The UVW2, UVW1, UVM2, B, U, V are the ultraviolet-optical filters of Swift.

Figure 1.4: The estimated time lags versus the corresponding wavelength, as given by Edelson et al. (2015).



They found that the optical and ultraviolet variations are strongly correlated, with correlation coefficients, r , larger than 0.57. Delays were detected between the observed variations in the different bands. The resulted time lag increases with the wavelength. On the contrary, the correlation between the X-rays and the ultraviolet radiation was not that high ($r < 0.45$), and the results about the corresponding time lag were inconclusive about which is the leading emission.

Figure 1.4 shows the plot of the resulted time lags (with respect to the HST variations) as a function of wavelength. The data points were fitted by the following function:

$$\tau = B \left[\left(\frac{\lambda}{\lambda_0} \right)^{4/3} - 1 \right] \quad (1.8)$$

where $\lambda_0 = 1367\text{\AA}$ is the central wavelength of the HST data (see E15 for more details). The red solid line in Fig. 1.4 denotes the best-fit line given by equation (1.8). The wavelength dependence of the time lag, i.e. $\tau \propto \lambda^{4/3}$, is the one expected in the case when the disk

is illuminated by the X-rays. In this case, the X-ray variations are expected to lead the ultraviolet-optical variations and the time lag should be determined by light-travel time between the central X-ray source and the disk regions where the optical-ultraviolet emission originates. The results of E15 are in agreement with those reported by McHardy et al. (2014), who also studied NGC 5548 variability using previous Swift observations.

1.5 The main objective of the study

The results presented by E15 suggest that the disk is illuminated by the central X-ray emission and the observed optical/UV flux variations are driven by the X-ray corona variability. However, an additional, surprising result of E15 was that the X-ray/ultraviolet correlation is rather low. This should not be the case, if indeed what we observe in NGC 5548 involves the X-ray illumination of the accretion disk. In fact, the low X-ray/UV-optical cross-correlation weakens the above picture.

One possibility that can explain the discrepancy is the following. As already mentioned, the observed X-ray flux in the energy range 0.2-10 keV² is a combination of the intrinsic X-ray emission of the central source and the interaction of this emission with the warm absorber. As a result, the observed X-ray variability should also be modulated by a rather complicated combination of the variability patterns of the two components. Therefore, one should first take into account the warm absorber's effects and estimate the intrinsic X-ray flux, before proceed to estimate the correlation between the ultraviolet emission and the X-rays.

The main objective of this work is exactly that. I intended to fit various models to the X-ray spectra, determine the intrinsic X-ray flux and then cross-correlate it with the ultraviolet lightcurves, to estimate the intrinsic X-ray/UV correlation in this object.

To this end, I used the Swift observations of NGC 5548 to extract the source's spectra and I fitted them with physical models that can account for the X-ray emission from the hot corona and for the photon interaction with the warm absorber. In this way, I was able to estimate the intrinsic X-ray flux of the nucleus and I calculated the correlation between the X-ray flux and the observed ultraviolet variations.

The structure of the thesis is as follows. In Chapter 2, I describe the Swift monitoring of NGC 5548 and the extraction of the spectra. In Chapter 3, I present the procedure I followed to fit the X-ray spectra and I describe in detail the model I used. Chapter 4 presents the results from the cross-correlation analysis and finally, Chapter 5 summarizes the conclusions of this work.

²the Swift X-ray instrument is sensitive to photons with energy within this range

Chapter 2

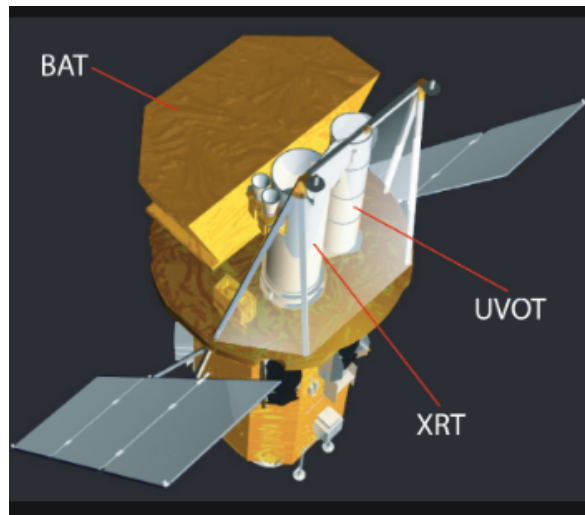
Data analysis

2.1 The 'SWIFT' mission

This work is based on the use of data collected by the 'Swift' observatory (Gehrels et al. 2004). I briefly describe its characteristics below.

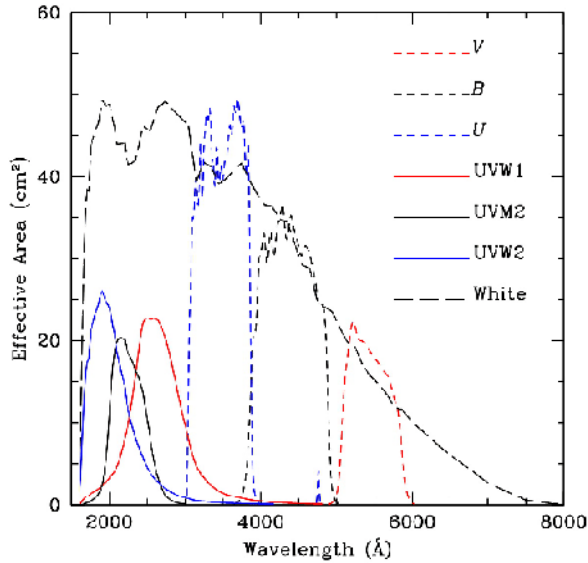
Swift (Fig. 2.1) is a low-Earth orbit satellite launched in 2004. It is part of NASA's "medium explorer" program and it was developed by an international team. The primary objective of the Swift mission was the observation of gamma-ray bursts. In addition to that, scientist have used Swift to observe many more celestial objects. Swift carries three co-aligned instruments: i) the Burst Alert Telescope (BAT), ii) the X-Ray Telescope (XRT) and iii) the Ultraviolet-Optical Telescope (UVOT), which, as indicated by their names, are sensitive to gamma-ray, X-ray, ultraviolet and optical wavelengths, respectively. The co-alignment of its instruments and their capability to work concurrently render Swift an ideal instrument for multiwavelength observations. In this work, I considered data collected by the XRT and UVOT only. The technical characteristics of those two instruments are given below. I did not consider BAT data because this instrument is sensitive to photons with energy bigger than 15 keV, and NGC 5548 is not luminous enough to be detected at these energies over a short time period.

Figure 2.1: An overview of the Swift telescope.



XRT: The Swift XRT (Burrows et al. 2005) is an X-ray telescope, which operates in the energy range between 0.2 and 10 keV. It has an effective area of 120 cm^2 at 1.5 keV. The XRT uses a Wolter 1 telescope to focus X-rays onto a 600×600 pixel CCD and its field of view is

Figure 2.2: The UVOT filters' response



23.6×23.6 arcminutes. The energy resolution of the instrument is rather moderate, since the Full Width at Half Maximum (FWHM) ranges from 50 eV at 0.1 keV to 140 eV at 6 keV and 190 eV at 10keV. The XRT can be operated in four modes: Imaging, Photodiode, Windowed Timing and the Photon-Counting mode. I used data retrieved in the latter mode, in which full spectral and spatial information is recorder, with a time resolution of 2.5 seconds.

UVOT: The UVOT (Roming et al. 2005) is a modified Ritchey-Chrétien telescope with 30 cm aperture and is sensitive to photons with $1700 \leq \lambda \leq 6000 \text{ \AA}$. When radiation enters UVOT, it is mirrored onto one of the two detector assemblies, which contains a photon counting CCD. The CCD has 256×256 pixels usable for scientific observations providing a field of view of 17×17 arcminutes. A filter wheel with six ultraviolet/optical filters is placed in front of each detector. The effective area of the system in each filter is plotted in Fig. 2.2.

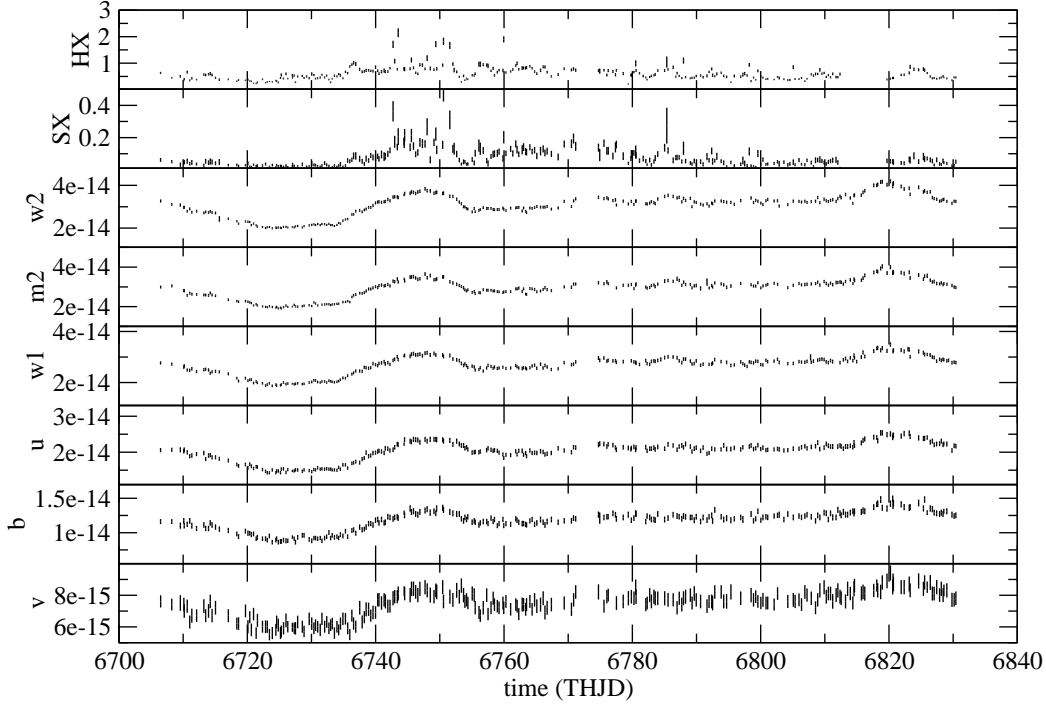
2.2 The Swift monitoring of NGC5548

NGC 5548 was intensively monitored by Swift from February 17 to June 22, 2014. During this time period, Swift observed the source 282 times resulting in a sampling rate better than one observation every ~ 0.5 day. There were 239 times that the source was observed in all the six UVOT filters (i.e. w2, m2, w1, u, b and v filter). The data reduction (Edelson et al. 2015) resulted in 1571 total UVOT usable data points.

The XRT monitoring resulted in 265 usable measurements. The observation that were conducted from 4, June to 10, June, 2014 were excluded from the analysis because the Swift XRT was in an anomalous state at that time. The mean exposure time of the XRT observations was 591 seconds. The lightcurves of the 6 UVOT filters fluxes and the X-rays are shown in Fig. 2.3. The X-rays have been divided into two groups, the hard X-rays (HX; 0.8–10 keV) and the soft X-rays (SX; 0.3–0.8 keV). The x-axis denotes time in units of

Truncated Heliocentric Julian Day (THJD), which is defined as $\text{THJD} = \text{HJD} - 2,450,000$, where HJD is the Heliocentric Julian Day.

Figure 2.3: The NGC lightcurve in the hard X-rays (HX), soft X-rays (SX) and the six UVOT filters (w2,m2,w1,u,b,v). The y-axis in the top two panels is in units of *counts/s* and in the other six panels is in units of $\text{erg}/(\text{s} \cdot \text{cm}^2 \text{\AA})$. The x-axis denotes the time in units of THJD.



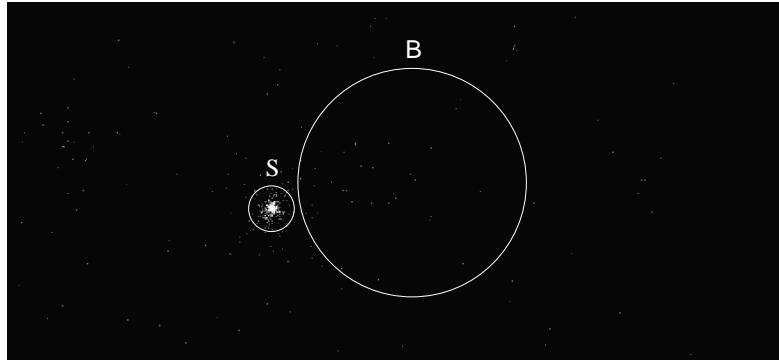
2.3 X-ray Data Reduction

I retrieved the X-ray Swift data from the HEASARC's database.¹ HEASARC is an acronym for the 'High Energy Astrophysics Science Archive Research Center', which is the primary data archive for high-energy astronomy space missions. The retrieved X-ray data files are in FITS format. They include information about the time, energy and position in detector's coordinates of the detected photons. I shall use these files in order to obtain the spectrum of NGC 5548, i.e. the flux of the source as a function of energy. To this end, I used the software package 'HEASOFT'. HEASOFT is a combination of the software packages *Xanadu* and *Ftools* and is used for multiwavelength astronomical data analysis.

¹<http://heasarc.gsfc.nasa.gov/cgi-bin/W3Browse/swift.pl>

At first, I used the *xrtpipeline* script. This perl script applies numerous tasks on the 'raw' data. Those tasks may include among others the removal of bad pixels, the selection of events based on the position of moon and sun, application of corrections to the detector coordinates etc. The outcome of the script is a number of files, such as the so-called "event" files and the exposure map of every observation.

Figure 2.4: The X-ray image of the sky area, where NGC 5548 is located. The 'S' and 'B' circles correspond to the source and background region, respectively (see text for details). The white dots indicate detected photons.



Spectrum extraction:

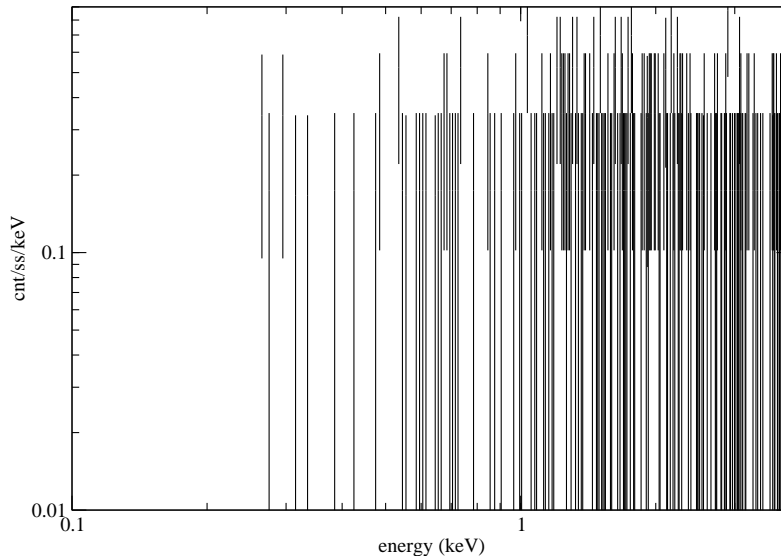
I used the *xselect* command and the event files to create an X-ray image for every observation. A typical example is shown in Fig. 2.4. Figure 2.4 corresponds to the observation performed on June 16, 2014 ($t = 6825.362$ THJD). The small circle indicates the sky position of NGC 5548 and the larger circle corresponds to the background region, which is defined below. The extraction of the spectrum for an observation corresponds to the computation of the source count rate for every CCD channel. This computation demands the definition of a "source region" on every image. The source region should be large enough to enclose most of the photons emitted by NGC 5548, while, at the same time, it should not be too extensive to avoid include many background photons, which leads to big errors. According to the 'Swift guidebook for XRT analysis', the 90% of the emission of an on-axis point source is enclosed by a 20 pixels radius circle. Therefore, I defined the source region to be a 20-pixel circle with NGC 5548 at its center. The *xselect* command uses the defined source region and the extracted image to produce the source spectrum for every observation.

Background subtraction:

However, the source region includes background photons, as well. For that reason, I must determine the background spectrum in order to subtract it from the spectrum I estimated using the source region. Thus, I defined a 'background region' and used it to extract the corresponding background spectrum. The background region should be source-free, near to

the AGN and as large as possible to allow for an accurate determination of the background level. I defined a circular background region with a radius of 100 pixels. Both the source and background regions are shown in Fig. 2.4 as "S" and "B" circles, respectively. To extract the background spectrum I once again used the *xselect* command. The background-corrected source spectrum for the observation of Fig. 2.4, is shown in Fig. 2.5. The signal-to-noise ratio is very low and the quality of the spectrum is poor.

Figure 2.5: The X-ray spectrum of NGC 5548 during the observation performed on June 16, 2014, at 20:35 (GMT).



Besides the spectrum files, two additional files are necessary to be used for a proper spectral analysis. Those are the Redistribution Matrix File (RMF) and the Ancillary Response File (ARF). The former accounts for the CCD quantum efficiency, which describes how a photon of given energy is redistributed into the output detector channel. While the latter contains all the rest response information, such as the effective area of the telescope, detector efficiency etc. RMF is provided in the Swift calibration database (CALDB). On the other hand, the ARF should be created individually for every observation. This is accomplished using the *xrtmkarf* command. *xrtmkarf* uses the exposure map created by *xrtpipeline* to take into account the bad pixels and bad columns of the CCD and creates an ARF. I used this command and the correspondig exposure maps to create an ARF for every single observation.

2.4 Observations Grouping

In order to increase the signal-to-noise ratio of the source spectra I grouped the observations into small groups, and I added their spectra together. The grouping was based on three criteria: 1) The total number of hard X-ray counts of all observations in each group should be larger than 1000. This number of photons was considered sufficient to produce high quality spectrum that can be used in reliable model fitting. 2) The observed hard X-rays

should not vary significantly among the observations of each group, and 3) the observations are successive. The last two criteria ensured that the loss of information regarding the source flux's time variability is minimized. The applying grouping resulted in 82 groups, typically one every ~ 1 -1.5 days. Despite the first criterion, there were 3 groups with total counts less than 900, and additional 4 groups had counts between 900 and 1000. This was the case when the count rate was significantly different between successive observations.

Figure 2.6: The hard X-ray lightcurve of NGC 5548. The indigo points correspond to the individual observations as given in Edelson et al.(2015). The black dots correspond to the mean count rate of the groups, as defined in the text. The horizontal "errors" indicate the time boundaries of each group.

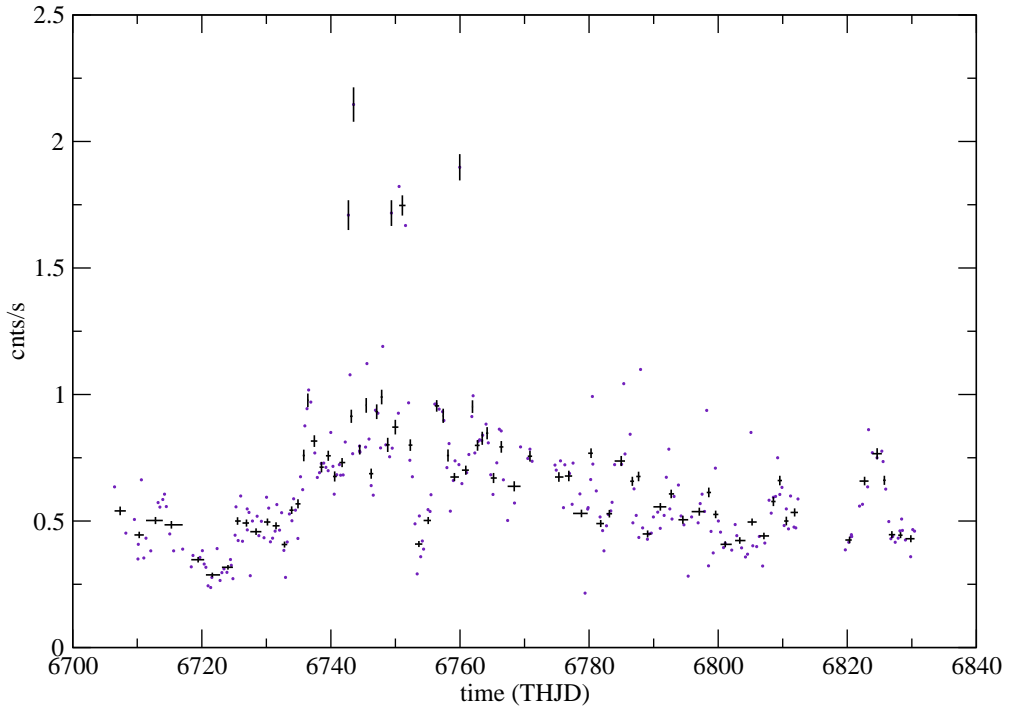


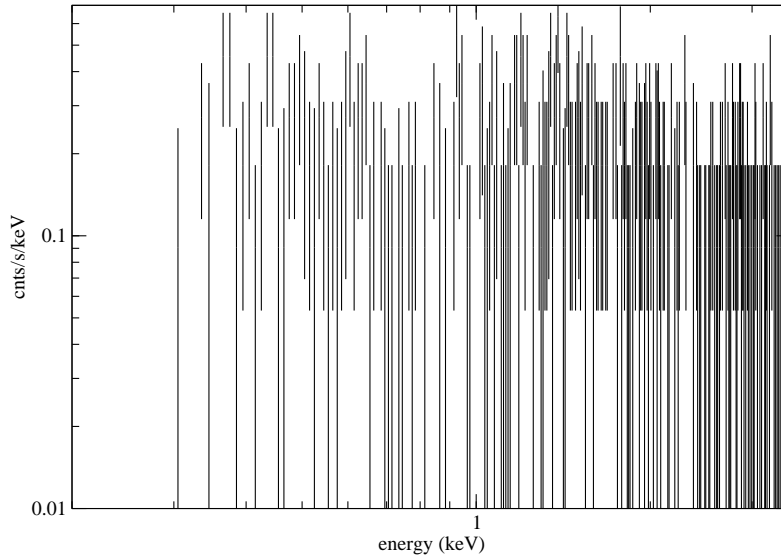
Figure 2.6 shows the hard X-ray lightcurve of the source. The indigo dots correspond to the observed count rate when no grouping is performed. In favor of clarity, their errors were omitted. The black dots indicate the hard X-ray flux of each group and the horizontal "error bars" represent the time boundaries of each group.

Adding the spectra:

Subsequently, I used the FTOOLS command *mathpha* to add the source spectra of each group's observations. This command performs mathematical operations on the spectrum files. I used it to compute the count rate in each bin of the total spectrum of each group. Before proceeding to analyze the spectra, I also need to create the corresponding RMF and ARF files. The RMF is common in all observation, and thus it can be used in the groups spectra

without any changes. On the opposite, a distinct ARF was created for each observation. As a result, I have to add those files properly in order to create the correct ARF for every group. The command that was used for that is called *addarf*. It takes as inputs the initial ARFs and a corresponding weight for each of them, and basically calculates a weighted mean of them. I used as weights the AGN’s hard X-ray count rate of each observation.

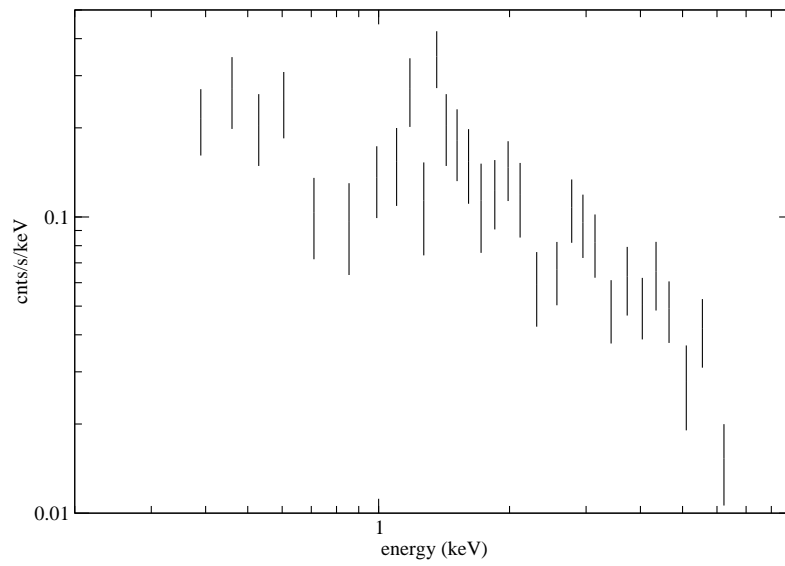
Figure 2.7: The X-ray spectrum of the 34th observation group. The axis are in logarithmic scale.



As an example, Fig. 2.7 shows the spectrum of the 34th group, which correspond to group time $t \simeq 6751$ THJD. This is the group with the maximum number of detected photons, namely 1931 cnts. Nevertheless, the signal-to-noise ratio per energy bin is still low.

In the foregoing analysis I intended to apply χ^2 fitting on the spectral data. This fitting method requires the error of each data point to be Gaussian. On the other hand, the photons follow a Poisson distribution. However, a Poisson distribution with mean value larger than ~ 15 can be approximately considered as a normal distribution. For that reason, I rebinned the spectrum of each group using the *grppha* command in such a way that there is at least 20 counts in every energy bin. The new spectrum of the 34th group is shown in Fig. 2.8.

Figure 2.8: The final X-ray spectrum of the 34th observation group. This spectrum is produced after the apply of the *grppha* command. Both the axes are in logarithmic scale.



These are the final spectra that are going to be used in the next chapter. In the following, I tried to find a proper physical model that fits well the spectrum of each group.

Chapter 3

X-ray Spectral Modelling

Having extracted the X-ray spectra (i.e. X-ray energy distribution, SED) of the source for each group, I tried to fit them with a theoretical model. I considered a model which comprises a Comptonization component and two extra components to account for the neutral and the warm absorbing effects. This is the most complicated model that can be used to fit the data. For the fitting process, I used 'XSPEC' (Arnaud 1996). XSPEC is part of the software package *Xanadu* and is a commonly used program to fit theoretical models on observed SEDs.

3.1 The X-ray model

The first model component I considered accounts for the photo-electric absorption of X-rays due to the Galactic interstellar medium (**wabs** in XSPEC terminology). I considered the absorption due to Milky Way's gas alone, and assumed no absorption in the host galaxy. The model is determined by one parameter only, which is the Galactic Hydrogen column density, $N_{H,0}$. Towards NGC 5548, $N_{H,0}$ is equal to $1.6 \times 10^{20} \text{ cm}^{-2}$ (Kalberla et al. 2005).

The second model component used (**nthcomp**, Zdziarski et. al. 1996, Zycki et. al. 1999) describes the continuum spectrum produced by thermal Comptonization when photons pass through a region of high-energy electrons. It is assumed that the seed photons follow a multicolor-disk blackbody energy distribution. The **nthcomp** model has the following parameters: 1) the temperature of electron in the hot medium, T_e , 2) the asymptotic power-law photon index, Γ , 3) the temperature of the innermost region of the disk, T_{bb} , which characterizes the distribution of the seed photons, 4) the redshift of the source and 5) a normalization parameter.

The temperature T_e cannot be estimated accurately by fitting the SED produced by Swift XRT data, because its estimation depends on the detection of the energy cut-off of the spectrum, which is usually observed at high energies. For example, Lubinski et al. (2016) analyzed observations of 28 Seyfert galaxies and found that the T_e temperature ranges from 26 to 359 keV. The median of the sample was 48 keV. In addition, Ursini et al. (2015) have estimated the energy cut-off in NGC 5548 to be larger than 50 keV. As a result, the cut-off cannot be constrained with the present data and therefore, I decided to keep T_e fixed and equal to $T_e = 100$ keV. Note that none of the results presented in this work depends on the choice of T_e , as long as it is larger than 100 keV.

The final component accounts for the absorption of photons in ionized gas (Krongold et al. 2003), i.e. for the "warm" absorption. The parameters of this model ("**phase**", hereafter) are: 1) the ionization parameter, defined as $u = \frac{Q_{ion}}{4\pi R^2 n_H c}$ where Q_{ion} is the number of ionizing photons per second, R is the distance of the gas to the source, and n_H is the hydrogen density, 2) the equivalent hydrogen column density of the cloud along our line of sight, N_H , 3) the internal thermal velocity of the gas, 4) the outflow or inflow radial velocity of the gas along the line of sight, v_r and 5) the fraction of the source covered by the absorber, f_c . The

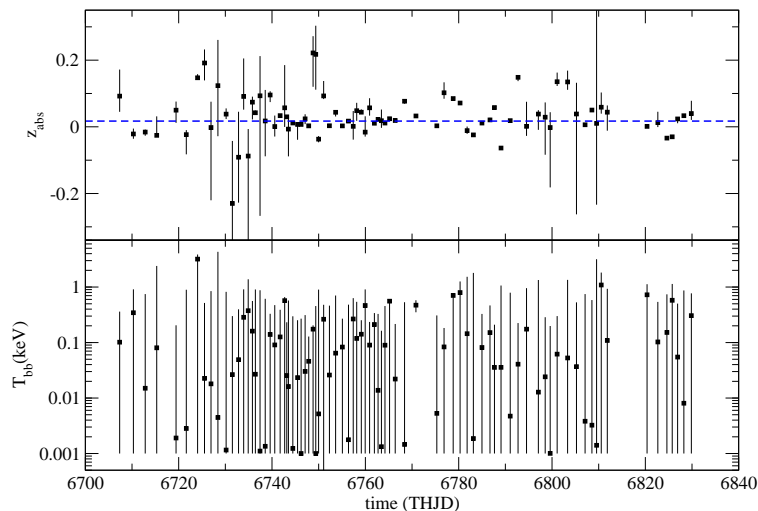
energy resolution of the spectra is not good enough to allow an accurate determination of the thermal velocity of the gas. Hence, I kept it fixed to a value of $300 \frac{\text{km}}{\text{s}}$ during the model fitting. It should also be mentioned that the radial velocity is expressed in terms of the redshift of the gas, z_{abs} . Assuming $v_r \ll c$, it turns out that $z_{abs} = (v_r + v_0)/c$ where v_0 is the velocity corresponds to the redshift of NGC 5548 and c is the speed of light. To sum up, the X-ray model in XSPEC terminology is `wabsnthcompphase`. Below, I describe the procedure I followed to fit the X-ray SED with this model.

3.2 Model fit: Stage 1

At first I fitted the SED with all the model parameters left free to vary (Model 1). This resulted to a good fit in terms of χ^2 , $\chi^2 = 2979.7$ for 2959 degrees of freedom (dof) and the corresponding null hypothesis (that the fit is good) probability is $P_{null} \simeq 0.39$. The degrees of freedom are defined as the total number of data points minus the model parameters left free to be determined during the fit. In the present case, the spectra have in total 3533 points or "bins".

Figure 3.1 shows the best-fit values of the warm absorber's redshift, z_{abs} , and the disk's inner temperature, T_{bb} . The redshift is unconstrained (i.e. its error are very large) in some of the observations and shows unphysically high variability among other periods. These "problems" are not unexpected given the low spectral resolution of Swift XRT, which does not allow a precise determination of the absorber's velocity. I also observed that T_{bb} is totally unconstrained. I concluded that neither of these parameters could be accurately estimated when they are left free to vary during the fitting procedure. I, therefore, decided to keep these two parameters fixed for all the spectra.

Figure 3.1: The best fit values of the warm absorber's redshift, z_{abs} , and disk temperature, T_{bb} , when all the parameters are left free to vary (model 1; upper and lower panel, respectively). The blue dashed line corresponds to the NGC 5548 redshift. The x-axis denotes time in units of Truncated Heliocentric Julian Day (THJD). The y-axis in the temperature diagram is in logarithmic scale.



3.3 Model fit: Stage 2

The weighted mean of the z_{abs} values plotted in Fig. 3.1 is $\bar{z}_{abs} = 0.0166 \pm 0.003$. This is consistent, within the errors, with the redshift of NGC 5548 ($z=0.017175$). Thus, I kept warm absorber's redshift equal to the AGN redshift, which is indicated by the dashed blue line in the upper panel of Fig. 3.1.

Regarding T_{bb} in order to determine the common value that I used in all the subsequent model fits, I linked the corresponding parameter for every group to the disk-blackbody temperature of the first group and I repeated the fit (Model 2). The best-fit disk temperature value is $T_{bb} = 67_{-66}^{+28}$ eV and the resulting best-fit χ^2 in this case was $\chi^2/\text{dof} = 3119.8/3122$. In order to examine if the current model fit was actually better than the previous fit, I used the F-test.

The F-test

The F-test (named after Ronald Fischer) is a statistical test used to compare two models that have been fitted to the same data set. Suppose a model fits the data, resulting in a χ^2 value of χ_1^2 , with df_1 degrees of freedom. Suppose now, that a second model is considered. This model is similar to the first one, except that, for some reason, during the fit, more model parameters are left free to vary. It is said that the first model is "nested" within the second. Assume also that the second model results in a χ^2 of χ_2^2 with df_2 degrees of freedom ($df_2 < df_1$). One way to compare and decide which of the two versions of the same model fits better the data is the application of the F-test. The F-value is defined as:

$$F = \frac{(\chi_1^2 - \chi_2^2)/(df_1 - df_2)}{\chi_2^2/df_2} \quad (3.1)$$

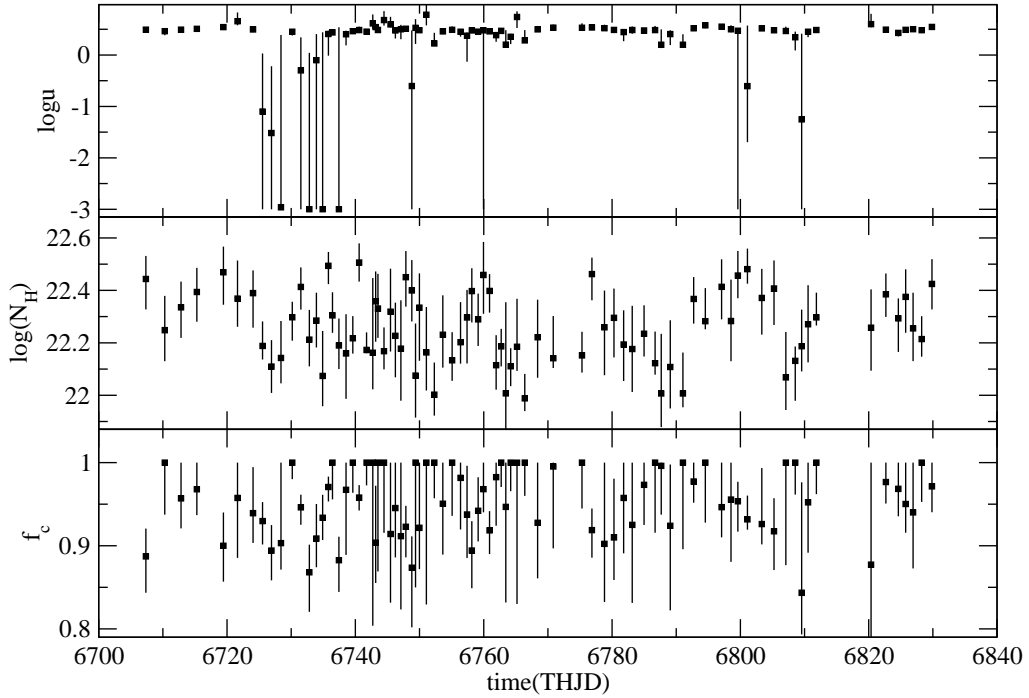
Under the null hypothesis that both the models describe equally well the data, the F-value should have an F distribution with $(df_1 - df_2, df_2)$ degrees of freedom. If the F-value is very large (i.e. if $P_{null} \ll 1$) then the more "complex" version of the model (the one with more free parameters) provides a significantly better description of the data. On the contrary, if the F-value is very small (i.e. if $P_{null} \sim 1$) then the simpler version is to be preferred.

I applied the above to compare Model 2 (when both z_{abs} and T_{bb} are not free) to Model 1. Using the values listed in Table 3.1 I found that the F-value is $F_{1,2} \simeq 0.85$, and hence, $P_{null} \simeq 0.91$. This indicates that Model 2 should be preferred over Model 1.

3.4 Model fit: Stage 3

Figure 3.2 shows the best-fit results for the **phase** model parameters, when both the redshift and T_{bb} were kept fixed. The ionization parameter, $\log \xi$, appears to be variable, although its best-fit values are highly uncertain in some cases. The N_H also exhibits variations up to a factor of 4, but its best-fit values have large uncertainties, as well. Finally, f_c does not seem to vary a lot. In fact, all the best-fit values are consistent with a value larger than 0.9, within the errors. In many cases, best-fit f_c is pegged at the largest allow value (of 1). The energy resolution of the spectra is not high enough, and so the fitting of the data with both the parameters f_c and N_H free is not conclusive on whether any of them is variable or not.

Figure 3.2: The best fit $\log u$ (upper), $\log N_H$ (middle) and f_c (bottom) values when z_{abs} and T_{bb} are fixed (Model 2). The x-axis denotes time in units of THJD.



In order to clarify the situation, I decided to re-fit the data two more times, keeping each time one of the two parameters free while linking the other to the value of the first group, as in the case of T_{bb} .

When f_c was kept the same for all groups (Model 3) the best fit resulted in a $\chi^2/\text{dof} = 3181.0/3204$. When N_H was linked (Model 4), the best fit resulted in $\chi^2/\text{dof} = 3211.3/3204$. Then, I used the F-test, as described in the previous section, to examine if any of these two models is statistically better than Model 2. I found that in the case of a constant f_c the null hypothesis probability of F-test was $P_{null} \simeq 0.96$, which suggests that it is statistically preferable to keep the covering factor constant. Moreover, the null hypothesis probability for Model 4 was $P_{null} \simeq 0.22$, which indicates that Model 2 and Model 4 fit equally well the data.

The F-test results suggest that both models 3 and 4 might be preferred to Model 2. To determine which of the two models (Model 3 and Model 4) should be used I had to examine which of them provides a better fit. Those two models cannot be compared using the F-test because none of them can be considered as a nested model of the other. One way I could follow to compare the two models is to use the concept of the "corrected" Akaike Information Criterion, AIC_c , which is defined by the equation:

$$AIC_c = 2k - 2C_L + \chi^2 + \frac{2k(k+1)}{N-k-1} \quad (3.2)$$

where k is the number of free model parameters, which in both models is $k=329$. N is the

number of data points, $N=3533$, and C_L is the likelihood of the true hypothetical model. C_L is the same in both the tested models. The model with the smallest AIC_c value is usually the preferred one. I used the above equation to calculate the difference of the two AIC_c values, $\Delta[AIC_c] = AIC_{c,4} - AIC_{c,3} = \Delta\chi^2 = 30.3$, where the numerical indices indicate the corresponding model for each AIC_c . Since the difference is larger than 10, it is strongly supported that the model with the lowest AIC_c , i.e. Model 3, is the best model. I also estimated the so-called "evidence ratio" for the model with the highest AIC_c (i.e. Model 4), which is defined as:

$$\epsilon_4 = e^{-\Delta[AIC_c]/2} \simeq 2.6 \cdot 10^{-7} \quad (3.3)$$

The evidence ratio is a measure of the likelihood that Model 3 would provide such a better fit (i.e. would have so smaller best-fit χ^2) under the assumption that Model 4 is the correct (true) model. It is evident that Model 3 is the one to be preferred.

Furthermore, I considered the case of both, N_H and f_c , being linked simultaneously (Model 5). The resulted χ^2 is 3287.5 for 3285 degrees of freedom. I used the F-test to compare this model to the one in which only the covering factor was held constant (i.e. Model 3). The corresponding probability for the new model to be significantly better is low, ~ 0.03 , and this led to the rejection of the new model. This indicates that the variations of N_H are real.

Table 3.1: A summary of the models considered in sections 3.2 to 3.4. The second column lists the parameters that were left free to vary during each model fit and the third column lists the resulted best-fit χ^2 . The corresponding null hypothesis probability is listed in column 4.

Model	Free Parameters	χ^2/dof	$P_{null}(\%)$
1	$z_{abs}, T_{bb}, f_c, \Gamma, \text{norm}, N_H, u$	2979.7 / 2959	39
2	$f_c, \Gamma, \text{norm}, N_H, u$	3119.8 / 3122	51
3	$\Gamma, \text{norm}, N_H, u$	3181.0 / 3204	61
4	$\Gamma, \text{norm}, u, f_c$	3211.3 / 3204	46
5	Γ, norm, u	3287.5 / 3285	48

To recapitulate, I used the model `wabs.nthcomp.phase` to fit the X-ray spectra. In the procedure of fitting I found that the model parameters z_{abs} , T_{bb} and f_c should be kept fixed. The warm absorber's redshift is assumed equal to the NGC 5548 redshift, while the other two parameters were determined by linking them to the parameters of the first group and are equal to $T_{bb} = 67_{-66}^{+28} eV$ and $f_c = 0.958_{-0.002}^{+0.003}$. The only free parameters are the `nthcomp`'s Γ and normalization parameter, and the `phase`'s N_H and ionization parameter. The χ^2 of the final fit (when T_{bb} and f_c are frozen in all the spectra and not linked) was $\chi^2/\text{dof} = 3169.4/3205$ and the corresponding null hypothesis probability was $P_{null} \simeq 67\%$, which indicates a good fit and is statistically accepted. A summary of the models considered during the above procedure is given in Table 3.1. Table 3.1 also lists the resulted χ^2 and the corresponding null hypothesis probability for every model. The best-fit values for the 4 left to vary parameters are plotted in Fig. 3.3 and 3.4.

Figure 3.3: The best fit values of the nthcomp parameters. The upper panel shows the Γ values and the lower shows the normalization parameter. The x-axis denotes the time of the observation groups in units of THJD.

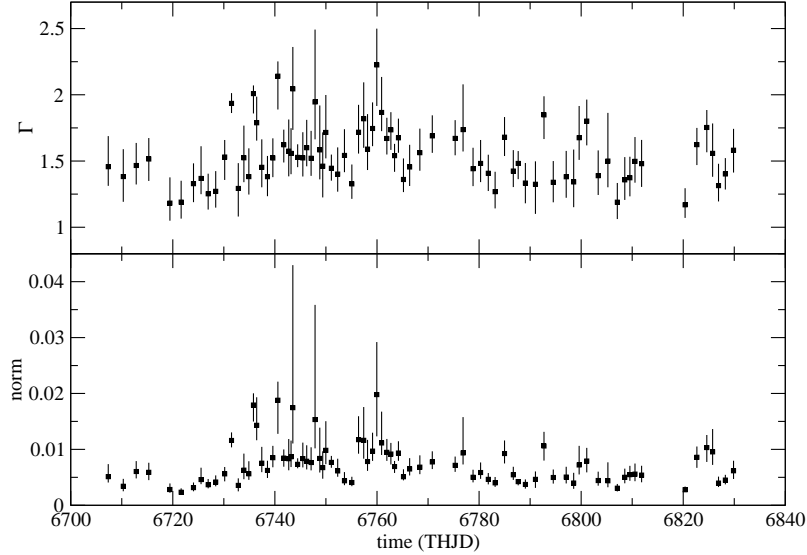
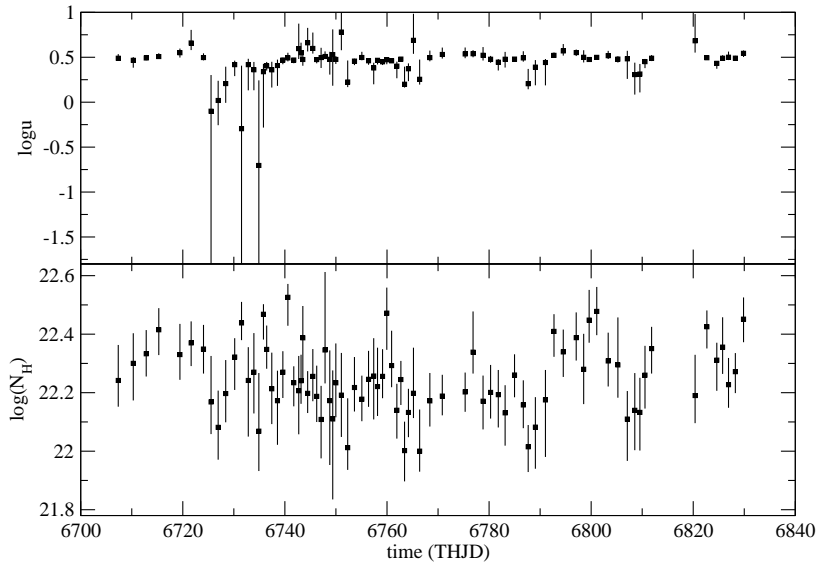


Figure 3.4: The best fit values of the phase parameters. The upper panel shows the ionization parameter and the lower shows the equivalent column density. The x-axis denotes the time of the observation groups in units of THJD.



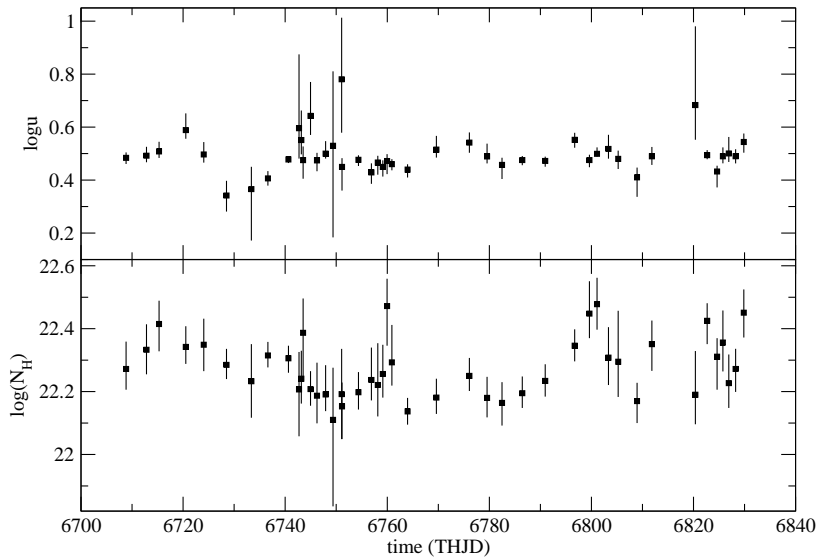
3.5 The warm absorber parameters

The only model parameters of `phase` that were finally left free to be minimized during the fit, are the ionization parameter, u , and the hydrogen column density, N_H . The best-fit values for the two parameters are shown in Fig. 3.4. A visual examination of this figure deduced

that both the parameters have large uncertainties and hence, need to be better determined.

I noticed that there were cases in which neighboring observation groups corresponded to a similar hard X-ray flux and, at the same time, their best-fit confidence intervals for the ionization parameters were highly overlapping. There were 21 such cases in total. I decided to repeat the fit in each of these cases, but now the phase parameters, u and N_H , were forced to be the same in all the neighboring groups. The procedure described above did not affect the quality of the fit significantly. The new χ^2 was 3260.2 for 3279 degrees of freedom. The plots of the new best-fit values are shown in Fig. 3.5.

Figure 3.5: The best fit values of the phase parameters when u and N_H were linked in some of the groups. The upper panel shows the ionization parameter and the lower panel shows the equivalent column density. The x-axis denotes time in units of THJD.



3.6 The X-ray continuum model parameters

The previous section describes the procedure I followed in order to constrain the best-fit values for the phase parameters. This procedure also resulted in different best-fit values for the Γ and normalization parameter of `nthcomp` model, which are shown in Fig. 3.6

Some of the new best-fit Γ and normalization values, plotted in Fig. 3.6, still have large errors. In order to better determine those parameters, I grouped the values with the larger uncertainties and calculated the weighted mean of each group for both of the parameters. Each mean is calculated by successive in time values. There were 22 values that were grouped in 8 different groups. The grouping is further specified in Table 3.2. The final results are shown in Fig. 3.7.

Figure 3.6: The best fit values of the nthcomp parameters when u and N_H were linked in some of the groups (see text). The upper panel shows the Γ values and the lower shows the normalization parameter. The x-axis denotes the time of the observation groups in units of THJD.

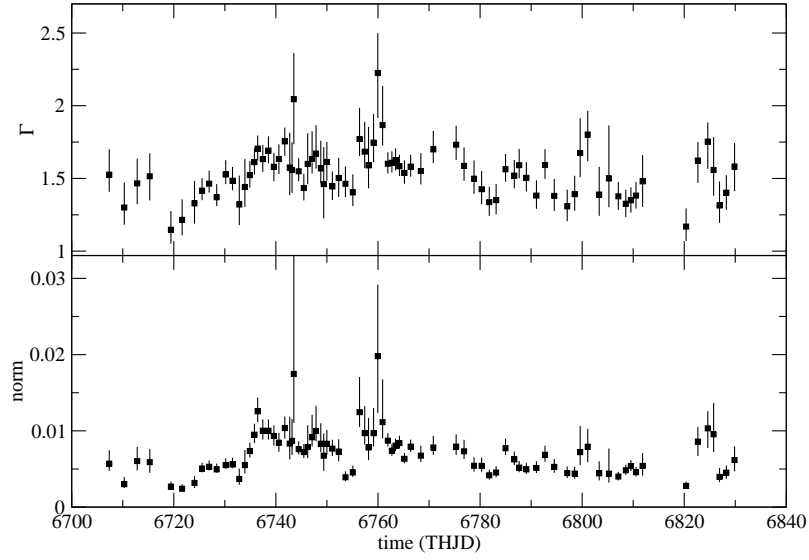


Figure 3.7: The final best fit values of the nthcomp parameters. The top panel shows the Γ values and the bottom panel shows the normalization parameter. The x-axis denotes the time of the observation groups in units of THJD.

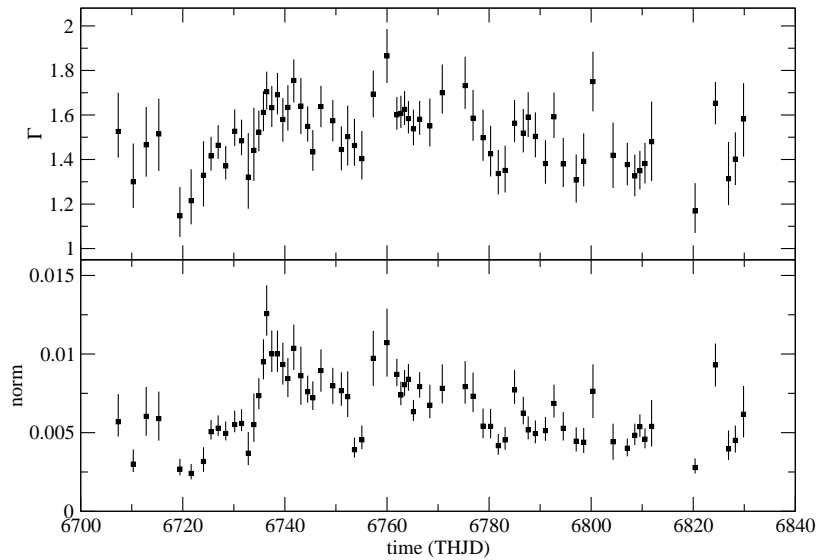


Table 3.2: The grouping of the best fit Γ and normalization values (Fig.3.6; see text for details). The second column indicates the number of best-fit values that were used to calculate the corresponding weighted mean. The third column indicates the time interval of each group in units of THJD.

# of group	values in the group	time (THJD; from - until)
1	3	6742.713 – 6743.510
2	3	6746.236 – 6747.861
3	3	6748.802 – 6749.979
4	3	6756.388 – 6758.144
5	3	6759.135 – 6760.902
6	2	6799.604 – 6801.094
7	2	6803.343 – 6805.246
8	3	6822.679 – 6825.753

Chapter 4

Correlation analysis

In this chapter I present the results from the correlation study between the intrinsic X-ray flux and the ultraviolet variations as well as between some of the model parameters. The correlations were quantified by estimating the so-called "cross-correlation function" between the two time series. Therefore, I present below a brief introduction to the cross-correlation functions.

4.1 The Cross-Correlation Function

The Cross-Correlation functions are a useful analysis tool when looking for similarities or differences amongst different time series. Assuming that X and Y are two random variables, the classical "covariance function" between them is defined as:

$$\text{cov}\{X(t), Y(t + \tau)\} = E \{[X(t) - \mu_X][Y(t + \tau) - \mu_Y]\} \quad (4.1)$$

where μ_X and μ_Y denote the mean values of the random variables. $E\{f\}$ is the expected value of the function f and τ is the so-called "time lag" (or simply the delay). The covariance function measures the degree to which X and Y deviate from their mean in a similar way at a time difference τ . If $X(t)$ and $Y(t + \tau)$ deviate from μ_X and μ_Y in a similar way, then the covariance function will be positive, on average. If they deviate in an opposite way the covariance function will be negative.

It can be shown that if $X(t)$ and $Y(t)$ are stationary, then the covariance function depends only on τ . Moreover, for a single random variable the $\text{cov}\{X(t), Y(t + \tau)\}$ is called as the auto-covariance function. It indicates whether there are "repeated trends" in the time series (i.e. if there is "memory" in the process). The covariance between two different random variables is called as the cross-covariance function.

In addition to $\text{cov}\{X(t), Y(t + \tau)\}$, one may also define the "correlation function" as:

$$CF(\tau) = \frac{E \{[X(t) - \mu_X][Y(t + \tau) - \mu_Y]\}}{\sigma_X \sigma_Y} \quad (4.2)$$

where σ_X , σ_Y are the standard deviations of X and Y , respectively. Again, for a single variable, the CF is called as the "auto-correlation" function (ACF); otherwise it is called as the "cross-correlation" function (CCF). The correlation function can be thought as the normalized covariance function with respect to the zero-lag covariance (i.e $\tau = 0$). If the two time series are positively and linearly correlated (with a time difference τ), then at this same lag the cross-correlation function is $CCF=1$. If they are negatively and linearly associated, then $CCF=-1$; and if the two processes are not correlated, then $CCF=0$ at all time lags.

The "Discrete Correlation Function"

The CCF, can be easily estimated when the two data samples are evenly spaced in time. However, the astronomical data do not usually fullfil the above restriction. Moreover, one should take into account the experimental uncertainties of the measured data. As a result, Endelson and Krolik (1988) introduced the Discrete Correlation Function (DCF) method in order to estimate the CCF between two astronomical time series. Its definition is clarified below.

Assuming that x and y are two data series, one can use every pair (x_i, y_j) to calculate the corresponding unbinned discrete correlations:

$$UDCF_{ij} = \frac{(x_i - \bar{x})(y_j - \bar{y})}{\sqrt{(\sigma_x^2 - e_x^2)(\sigma_y^2 - e_y^2)}} \quad (4.3)$$

where the bar denotes the mean value of each sample and e^2 is the "mean-square error" defined for every data sample as:

$$e^2 = \frac{1}{N} \sum_{i=1}^N \sigma_{err,i}^2 \quad (4.4)$$

N is the total number of data points for each series and $\sigma_{err,i}$ is the experimental error of each data point. The difference $\sigma^2 - e^2$ used in equation (4.3) is called "excess variance" (Nandra et al. 1997; Vaughan et al. 2003) and is indicative of the true variance of an observed time series, since it takes into account the variability introduced by the measurement errors, e^2 .

Each $UDCF_{ij}$ is associated with a corresponding time lag $\Delta t_{ij} = t_j - t_i$. The "Discrete Correlation Function" is defined by the relation:

$$DCF(\tau) = \frac{1}{M} \sum' UDCF_{ij} \quad (4.5)$$

The symbol \sum' denotes sum over all the M pairs (α_i, b_j) with time intervals Δt_{ij} such that: $\tau - \frac{\Delta\tau}{2} \leq \Delta t_{ij} \leq \tau + \frac{\Delta\tau}{2}$. $\Delta\tau$ defines the bin width of the estimated DCF. A measure of the uncertainty of the DCF, is given by:

$$\sigma_{DCF}(\tau) = \frac{1}{M-1} \left\{ \sum' [UDCF_{ij} - DFC(\tau)]^2 \right\}^{1/2} \quad (4.6)$$

The above equation is only approximate, as the individual $UDCF_{ij}$ within each bin are correlated in most cases.

4.2 The intrinsic X-ray/UV correlation in NGC 5548

As mentioned in Section 1.4, the main objective of my work is to estimate the CCF between the intrinsic X-ray flux and the observed ultraviolet continuum variations. According to the modelling of the X-ray spectra, the intrinsic X-ray emission is determined by the `nthcomp` flux. Using the `nthcomp` best-fit results, I can in principle estimate the X-ray flux at each time. However this is not an easy task. The X-ray spectra span a small energy range

(approximately 0.3–10keV) and I fitted the data using a complex model. As a result, the best-fit Γ and `nthcomp` norm (n_{nth}) values have rather large uncertainties. Consequently the use of these parameters to estimate the full band flux will result in measurements with large uncertainties, due to the large uncertainties of the best-fit model parameters.

Another possibility is to adopt the n_{nth} values as representative of the intrinsic X-ray variations. But, since both n_{nth} and Γ are variable, the intrinsic X-ray flux variations depend on the Γ variations as well. To clarify the situation, I calculated the fractional root mean square variability amplitude, F_{rms} , of both Γ and n_{nth} . This quantity is defined as (Vaughan et al. 2003):

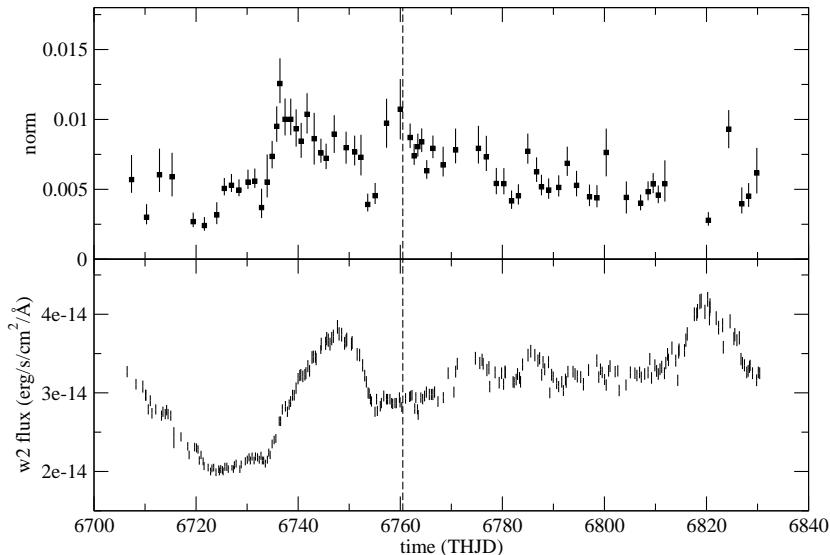
$$F_{rms} = \sqrt{\frac{\sigma^2 - e^2}{\bar{f}}} \quad (4.7)$$

where σ denotes the standard deviation of the lightcurves and e^2 is the corresponding mean-square error (equation 4.4). F_{rms} indicates the fractional intrinsic variability amplitude for each parameter with respect to their mean value. I found that:

$$F_{var,norm} = 0.29 \quad \text{and} \quad F_{var,\Gamma} = 0.06$$

The normalization parameter is significantly more variable than Γ . Therefore, it is reasonable to consider that the variability of the X-ray flux should be mainly determined by the normalization variability.

Figure 4.1: The lightcurves of the normalization parameter and w2-filter flux (upper and lower panel, respectively). The vertical dashed line corresponds the boundary between the two parts of the lightcurves (see text for details). The x-axis denotes time in units of THJD.



I, thus, proceeded to calculate the DCF between the `nthcomp` n_{nth} and the ultraviolet flux observed in the w2 filter of Swift UVOT, in order to determine the intrinsic X-ray/ultraviolet correlation in NGC 5548. The ultraviolet flux lightcurve is shown in the bottom panel of Fig.

4.1. The top panel shows the time evolution of n_{nth} (hereafter, I will refer to this plot as the "intrinsic" X-ray lightcurve). I used equation (4.5), with $\Delta\tau = 1day$, to estimate the CCF.

At first, I considered the full monitoring period from 6706 to 6831 THJD (i.e. from February 17 to June 22, 2014). The left panel of Fig. 4.2 shows the resulting DCF (black circles). The blue squares show the sample DCF between the observed hard X-ray and the w2 count rates. I noticed that the maximum DCF, DCF_{max} , is approximately the same in both cases. This result shows that the strength of the X-ray/UV correlation does not improve even when I consider the intrinsic X-ray flux. To estimate the delay, I calculated the centroid of the time lag results, $\tau_{centroid}$, which is defined as the mean value of the lags that correspond to $DCF > 0.75 \times DCF_{max}$. I found that $\tau_{centroid} \simeq -5.9days$, with the X-rays leading the UV variations. This is significantly larger when compared to the lag in the DCF of the observed UV and X-ray count rates.

In order to estimate an error on $\tau_{centroid}$ and DCF_{max} , I followed the method described in Peterson et al. (1998). This method is based on Monte carlo simulations. In each iteration, one determines a subset for each of the lightcurves. The subset consists of points of the initial set ($\sim 70\%$ of the initial points) that were randomly picked without regard to whether they had been previously selected or not. Then, I computed the DCF, and for each set I estimated a new $\tau_{centroid}$ and DCF_{max} . After the execution of 10000 iterations, the sample τ_{peak} and DCF_{max} values can be used to determine their distribution, which I considered as representative of the true distribution of these parameters.

Figure 4.2: The DCF between intrinsic X-rays and the ultraviolet flux (left panel). The black circles correspond to the DCF between n_{nth} and the w2-filter flux, while the blue squares correspond to the DCF between the observed hard X-ray and w2-filter count rates. The right panels show the histogram of $\tau_{centroid}$ and of DCF_{max} , based on the simulations that I did to estimate the $\tau_{centroid}$ and DCF_{max} error (see § 4.2).

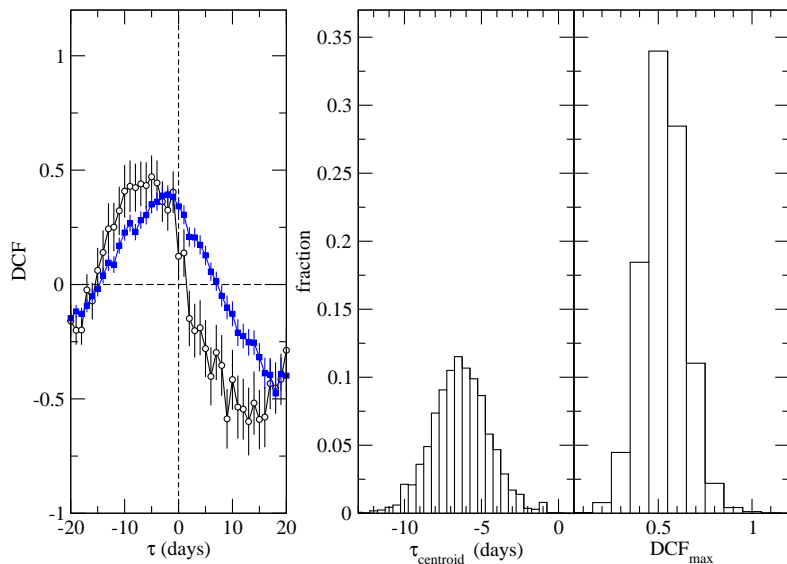


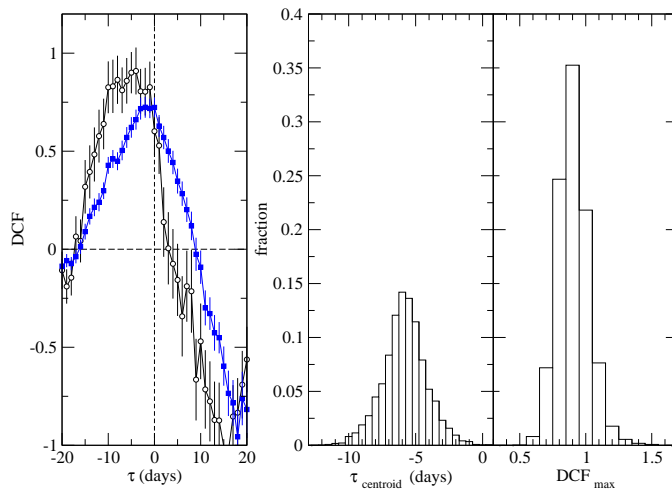
Figure 4.2 shows the resulting distributions of $\tau_{centroid}$ and DCF_{max} (right-hand panels).

Using these results, I found that the 90% confidence intervals of $\tau_{centroid}$ and DCF_{max} are -8.0 to -3.3 days and 0.35 to 0.72, respectively.

My results suggest that the corona emission leads the ultraviolet emission by a time lag, $\tau \sim 6days$. However, as I mentioned above, the value of the corresponding DCF is still rather small. A visual examination of the lightcurves plotted in Fig. 4.1, indicates that the w2 flux and intrinsic X-rays are rather well correlated during the first half of the monitoring campaign. A "flare"-like event is observed in both lightcurves from ~ 6730 to ~ 6750 THJD. The X-ray flux appears to increase at ~ 6725 THJD, reaching a maximum value at ~ 6735 THJD and then decays slowly. A similar flux rise in the ultraviolet band is observed at ~ 6730 THJD, reaching maximum at ~ 6745 THJD. At later times (after ~ 6760 THJD) the ultraviolet and X-ray variations appear to be un-correlated. In fact the ultraviolet flux appears to increase on average during this period, while the X-ray flux appears to decrease.

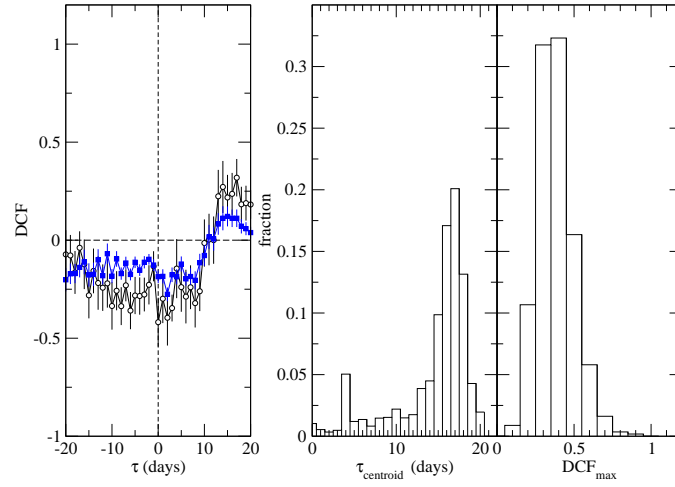
This led me to divide the lightcurves into two parts. The first part extends from 6706 to 6761 THJD and comprises the "flare"-like event in both lightcurves, while the second part lasts from 6761 to 6831 THJD. The dashed vertical line of Fig. 4.1 indicates the boundary date between the two parts. I then estimated the CCF between the n_{nth} values and the w2-filter flux for both parts.

Figure 4.3: As in Fig. 4.2, in the case when I estimated the DCF using only the first part of the lightcurves (see text for details)



Figures 4.3 and 4.4 show the correlation results when the two parts of observations are considered separately. These results verify that the variations of the two lightcurves (see Fig 4.1) are indeed well correlated during the first half period of observations and are almost uncorrelated during the second period. Furthermore, despite the strongest correlation coefficient in the first part, the resulted time lag is again large. Namely, $\tau_{centroid} \simeq -5.5days$, with a 90% confidence interval from -8.6 to -3.0 days.

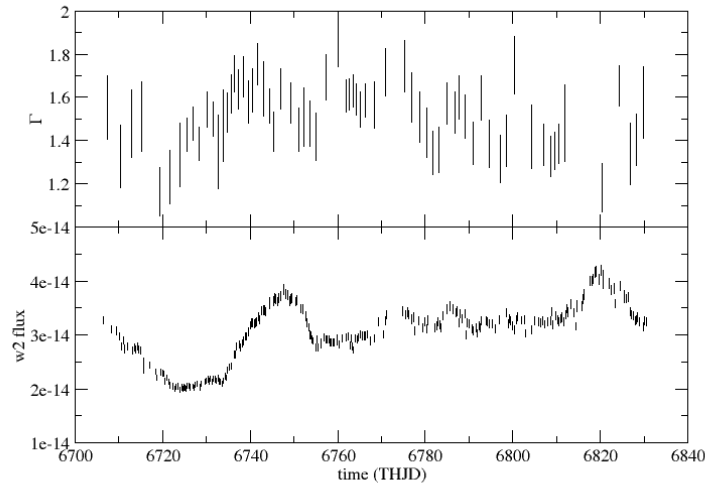
Figure 4.4: As in Fig. 4.2, in the case when I estimated the DCF using only the second part of the lightcurves



4.3 The Γ /UV correlation in NGC 5548

Then, I considered the correlation between the variations of the spectral index, Γ , and of the ultraviolet flux. The lightcurves of the two quantities are shown in Fig. 4.5.

Figure 4.5: The lightcurves of the spectral index Γ and w2-filter flux (upper and lower panel, respectively)



If the ultraviolet photons are the soft input photons to the X-ray corona, then I would expect the two lightcurves of Fig. 4.5 to be well correlated, with the ultraviolet variations leading the Γ variations. Such correlations have been already observed in previous studies (see for example Nandra et al. 2000). To examine if this is the case in NGC 5548, I estimated

the CCF between the ultraviolet flux and Γ . The results are shown in Fig. 4.6

Figure 4.6: The DCF results between the ultraviolet flux and Γ .

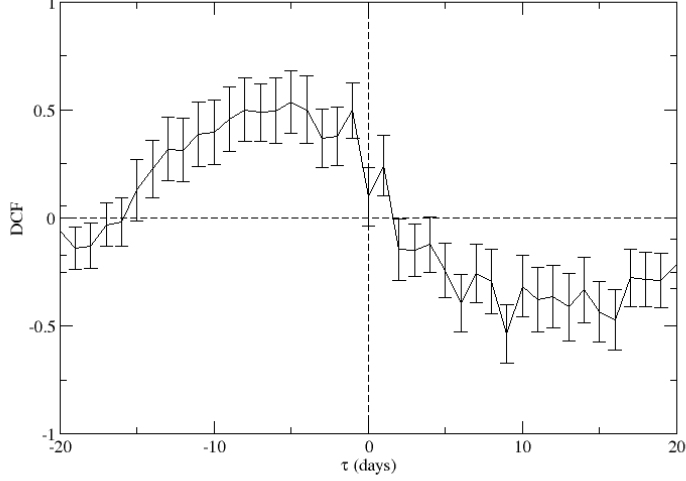
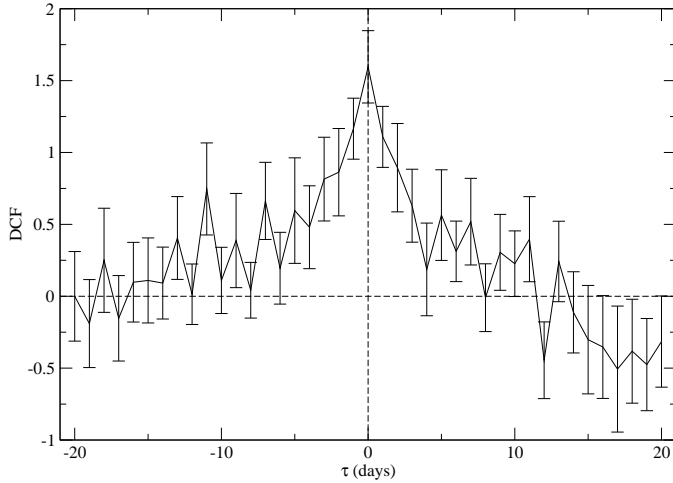


Figure 4.6 shows that the correlation between Γ and ultraviolet count rate variations is rather low, $DCF_{max} \simeq 0.49$, and at the same time, the Γ variations lead the ultraviolet variations with a delay of $\tau_{centroid} \simeq 5.7$ days. There is no obvious physical explanation for this result.

Figure 4.7: The DCF results between the n_{nth} and Γ parameters.



The observed correlation is probably not intrinsic, but a by-product of two other observed correlations. As I have discussed, the observed ultraviolet flux is correlated with the intrinsic X-rays, with a resulting time delay $\tau_{centroid} \simeq -5.9$ days and a correlation coefficient $DCF_{max} \simeq 0.42$ (see § 4.2). In addition to that, there is a significant correlation between the intrinsic X-rays and Γ . This is clearly seen in Fig. 4.7, which shows the correlation results between Γ and n_{nth} . The two variables are highly correlated with a maximum DCF at zero time lag (the fact that the correlation function exceeds 1 near zero lag is almost certainly due

to an overestimate of the two variables). These two correlations could explain the correlation I observed between Γ and the ultraviolet flux. This strongly suggests that the ultraviolet flux observed in Swift's w2 filter (which has an effective wavelength $\lambda_{eff} = 2030\text{\AA}$) is not the source of the soft photons that are upscattered to X-rays.

Chapter 5

Summary and Conclusions

5.1 Summary of the work

In this work I investigated the correlation between the intrinsic X-ray flux and the observed ultraviolet flux of the active galactic nucleus named NGC 5548. To that end, I analyzed the observations of this object that were obtained by the Swift observatory from February to June, 2014. Swift observed NGC 5548 ~ 265 times, resulting in a sampling rate ~ 2 observations every day. This campaign is one of the densest ever conducted for an AGN.

At first, I followed the standard procedure to extract the X-ray spectra of the source. I divided the observations into groups, with each group containing typically 2–4 successive observations. There were in total 82 groups, typically one group every ~ 1 –1.5 days. I fitted those spectra with a "proper" theoretical model. It is generally accepted that the observed X-rays of an AGN in the energy range 0.3–10 keV are mainly the result of two processes. The first process corresponds to the production of X-ray photons by thermal Comptonization and is considered to be the intrinsic X-ray source of an AGN. The emitted X-ray photons interact with a photo-ionizing gas, which is commonly called warm absorber. This interaction is the second process that contributes in the observed flux. Therefore, the considered model accounts for both the thermal Comptonization of soft photons (`nthcomp` in *XSPEC*) plus absorbing by the warm absorber (`phase` in *XSPEC*). I fitted different versions of this same model to the spectra in order to determine the variable physical parameters of the system. I found that only four parameters showed variability, namely the spectral photon index Γ , the normalization parameter, n_{nth} , of `nthcomp`, the ionization parameter and the hydrogen column density of the warm absorber.

The model parameters of the Comptonization component can be used to estimate the intrinsic X-ray flux, but this is not an easy task. Both parameters, Γ and n_{nth} , were estimated over a narrow energy band and have large uncertainties. Thus, their extrapolation in order to determine the full-band X-ray flux would result in estimates with large uncertainties. Both parameters are also variable, with n_{nth} be the most variable. So I decided to use the best-fit values of n_{nth} as a proxy for the intrinsic X-rays variations.

After that, I examined the correlation between the intrinsic X-rays and the ultraviolet flux. The resulted correlation was rather low ($DCF_{max} \simeq 0.45$). The strength of the correlation is in agreement with the correlation found by Edelson et al. (2015) when they correlated the observed X-ray count rate with the w2 lightcurve.

However, I estimated that the corresponding timelag between the variations in the two bands is ~ 6 days, with the X-rays leading the ultraviolet emission. This is significantly larger than the timelag calculated by E15 (~ 1 day) and other previous studies as well. In fact, E15 calculated a time delay of $\tau_{centroid} = 1.06 \pm 0.49$ days, while I estimated that $\tau_{centroid} = 5.9$ days, with a 90% confidence interval values from -8.0 to -3.3 days. The two results do not agree even when the resulted errors are taken into account .

Moreover, I noticed that the correlation between the intrinsic X-rays and the ultraviolet flux was significantly stronger in the first half of the observations than in the second one. Therefore, I decided to divide the sample of the X-ray flux into two parts as shown in Fig. 4.1 and to estimate the correlations in these parts independently. I found that the correlation in the first time period was significantly higher ($DCF_{max} \simeq 0.85$) than when I used the total sample, while the time lag was not affected significantly. In contrast, the fluxes in the second time period seem to be almost uncorrelated. The main difference between the two parts is that both lightcurves show a high-amplitude "flare"-like event in the first part. On the other hand, the variations in the second part are of relatively smaller amplitude in both lightcurves.

Finally, I calculated the correlation coefficient between the ultraviolet flux and the spectral index Γ . I found that the correlation between the two variables was small and that Γ variations appear to lead the ultraviolet emission variations. I would expect the opposite behaviour. If w2 photons are the soft input photons in the corona, then a rise in the ultraviolet emission would result in the increase of Γ , with a time delay (i.e. the ultraviolet variations lead the Γ variations); and correspondingly in the opposite case. This result may be an artifact due to the observed X-ray/ultraviolet correlation and the n_{nth}/Γ correlation, in which case the reduced correlation between the spectral index and the UV flux is not real.

5.2 Conclusions

As already mentioned above, the resulted UV/X-ray timelag is significantly larger when the intrinsic X-ray flux is considered. If this is indeed the case, the time lag cannot be explained by light-travel delay between the X-ray and the ultraviolet source. Such a large delay is not consistent with the wavelength dependence of the optical/ultraviolet delays that was presented by E15 (see their Fig. 4).

In addition to that, I found that the correlation is different in the two parts of the observed lightcurves. In particular, the correlation coefficient is significantly larger in the time period when a "flare"-like event was observed at the beginning of the monitoring campaign. This suggests that only significant variations can be propagated from the X-ray source to the ultraviolet one. On the contrary, less significant variations (i.e. variations with a smaller amplitude) do not appear to propagate between the two bands and, whatever their physical origin, they seem to be locally dissipated. Considering the large value resulted for the delay between the X-ray and UV, this "flare" event could be explained by accretion rate (\dot{m}) fluctuations originated in the inner region of the disk, where the X-ray source is located. Those fluctuations propagate both inwards and outwards, perhaps as sound waves, and thus variations in the ultraviolet-optical emission (which correspond to outer parts of the disk) are observed to occur at a much later time.

Finally, the lack of correlation between the ultraviolet variations and the spectral index Γ suggests that the photons detected in the w2 filter ($\lambda_{eff} = 2030\text{\AA}$) are not the soft photons that enter the hot plasma region and are Compton upscattered to X-rays. If this was the case, then the ultraviolet flux variations should lead the Γ variations. For example, an increase in the soft photons would cool down the corona temperature and would result in a steeper X-ray spectrum. A possible explanation for this result is that the soft photons are originated

in a region closer to the black hole and as a result they have higher energies than the photons observed in the w2 filter. This is indeed suggested by the spectral fit results, where the best-fit T_{bb} value was $T_{bb} \simeq 67eV$ (albeit with a large uncertainty). This temperature is much higher than the temperature expected in the inner disk assuming $M_{BH} \simeq 5 \times 10^7 M_{\odot}$, for moderate accretion rates. However, the soft input photons might be the result of thermal Comptonization of the underlining disk photons in a "warm" medium ($T \sim 0.2 - 0.5keV$) located just above the disk, as is suggested by other studies.

References

- Arnaud, K. A. 1996, *Astronomical Data Analysis Software and Systems V*, 101, 17
- Bentz, M. C., & Katz, S. 2015, *PASP*, 127, 67
- Burrows, D. N., Hill, J. E., Nousek, J. A., et al. 2005, *SSR*, 120, 165
- Crenshaw, D. M., Kraemer, S. B., Bogges, A., et al. 1999, *ApJ*, 516, 750
- Crenshaw, D. M., Kraemer, S. B., Gabel, J. R., et al. 2003, *ApJ*, 594, 116
- de Vaucouleurs, G., de Vaucouleurs, A., Corwin, H. G., Jr., et al. 1991, *Third Reference Catalogue of Bright Galaxies*. (Springer-Verlag: New York)
- Ebrero, J., Kaastra, J. S., Kriss, G. A., et al. 2016, *A&A*, 587, A129
- Edelson, R. A., & Krolik, J. H. 1988, *ApJ*, 333, 646
- Edelson, R., Gelbord, J. M., Horne, K., et al. 2015, *ApJ*, 806, 129
- Elvis, M., Wilkes, B. J., McDowell, J. C., et al. 1994, *ApJS*, 95, 1
- Gehrels, N., Chincarini, G., Giommi, P., et al. 2004, *ApJ*, 611, 1005
- George, I. M., Turner, T. J., Netzer, H., et al. 1998, *ApJS*, 114, 73
- Gondek, D., Zdziarski, A. A., Johnson, W. N., et al. 1996, *MNRAS*, 282, 646
- Kaastra, J. S., Kriss, G. A., Cappi, M., et al. 2014, *Sci*, 345, 64
- Kalberla, P. M. W., Burton, W. B., Hartmann, D., et al. 2005, *A&A*, 440, 775
- Krongold, Y., Nicastro, F., Brickhouse, N. S., et al. 2003, *ApJ*, 597, 832
- Lubiński, P., Beckmann, V., Gibaud, L., et al. 2016, *MNRAS*, 458, 2454
- McHardy, I. M., Cameron, D. T., Dwelly, T., et al. 2014, *MNRAS*, 444, 1469
- Nandra, K., George, I. M., Mushotzky, R. F., et al. 1997, *ApJ*, 476, 70
- Nandra, K., Le, T., George, I. M., et al. 2000, *ApJ*, 544, 734
- Peterson, B. M., Wanders, I., Horne, K., et al. 1998, *PASP*, 110, 660
- Roming, P. W. A., Kennedy, T. E., Mason, K. O., et al. 2005, *SSR*, 120, 95
- Steenbrugge, K. C., Kaastra, J. S., Crenshaw, D. M., et al. 2005, *A&A*, 434, 569
- Ursini, F., Boissay, R., Petrucci, P.-O., et al. 2015, *A&A*, 577, A38
- Vaughan, S., Edelson, R., Warwick, R. S., & Uttley, P. 2003, *MNRAS*, 345, 1271
- Zdziarski, A. A., Johnson, W. N., & Magdziarz, P. 1996, *MNRAS*, 283, 193
- Życki, P. T., Done, C., & Smith, D. A. 1999, *MNRAS*, 309, 561